Materials Science & Engineering A 953 (2026) 149747

Contents lists available at ScienceDirect

Materials Science & Engineering A

journal homepage: www.elsevier.com/locate/msea

Phase-selective transformation enabled coherent interfaces for coordinated deformation in FCC-Laves eutectic high-entropy alloys

Yusha Luo [a,b], Qihan Zheng [a,b], Bo Sun [a,b], Ruixin Sheng [a,b], Jinxiong Hou [c], Zhenzeng Chong [a,b], Qianqian Wang [a,b,*], Zhijun Guo [a,b], Zhe Jia [a,b], Yang Tong [d,**], Baolong Shen [a,b,***]

[a] School of Materials Science and Engineering, Jiangsu Key Laboratory for Advanced Metallic Materials, Southeast University, Nanjing, 211189, China
[b] Ministry of Education Key Laboratory of Structure and Thermal Protection for High-Speed Aircraft, Southeast University, Nanjing, 211189, China
[c] Department of Materials Science and Engineering, City University of Hong Kong, Hong Kong, 999077, China
[d] Advanced Studies in Precision Materials, Yantai University, Yantai, 264005, China

ARTICLE INFO

Keywords:
Eutectic high-entropy alloy
Coherent interface
Deformation mechanism
Generalized stacking fault energy
Phase-selective transformation

ABSTRACT

FCC-Laves eutectic high-entropy alloys (EHEAs) often exhibit brittleness due to mechanical disparity and incompatible interfaces between the soft FCC and hard Laves lamellae. In this study, we report an aging-driven phase-selective transformation approach to develop coherent interfaces in FCC-Laves EHEAs. After aging for 6 h (AG-6h alloy), the brittle Laves phase transforms into deformable $D0_{22}$ lamellae, converting semi-coherent FCC-Laves interfaces to coherent FCC-$D0_{22}$ boundaries. Simultaneously, coherent $L1_2$ precipitates form within the FCC lamellae. This structural evolution leads to doubled compressive plasticity (~12 %) and elevated strength (~3000 MPa) compared to the suction-casted alloy. First-principles calculations reveal that the phase-selective transformations of $(Ni_{14}Co_8Fe_1Cr_1)(Ta_6Cr_1Fe_1)$-$D0_{22}$ and cubical $(Co_9Ni_8Fe_5Cr_2)(Ta_3Cr_2Fe_3)$-$L1_2$ precipitates are thermodynamically favorable and enable interfaces coherent with the FCC matrix. The newly formed coherent FCC-$D0_{22}$ and FCC-$L1_2$ interfaces promote strain partitioning between adjacent lamellae under high stress. Consequently, the deformation mode changed from planar slips and stacking faults (SFs) in the suction-cast alloy to a coordinated mechanism in AG-6h alloy, involving dislocations with SFs in both FCC and $D0_{22}$ phases, along with deformation twins within the $D0_{22}$ phase. The competition between various deformation micro-mechanism modes is studied by transmission electron microscope and discussed based on generalized stacking fault energy curves. The phase-selective transformation strategy opens new perspectives for designing novel FCC-Laves EHEAs with low-misfit interfaces and high performance.

1. Introduction

Eutectic alloys, such as cast irons and casting aluminum alloys, have long been extensively employed across various industries, including electronics, automotive, and aerospace [1–4]. Unlike single-phase alloys, competitive solidification between dual or multiple phases endows them delicate microstructure, free segregation, excellent castability, and superior mechanical performance [5,6]. As a newly developed subclass, eutectic high-entropy alloys (EHEAs) designed by integrating the eutectic concept and multi-principal composition strategy, have garnered attention due to their superior strength-plasticity balance [5, 7–10]. Generally, the overall mechanical performance of EHEAs is primarily governed by a complex interplay of microstructural features, including the crystal structure, mechanical properties, volume fraction, morphology of the constituent phases, as well as lamellar spacing and interfacial characteristics [8,11–14]. These microstructural factors offer distinct pathways for microstructural tailoring and mechanical property optimization.

* Corresponding author. School of Materials Science and Engineering, Jiangsu Key Laboratory for Advanced Metallic Materials, Southeast University, Nanjing, 211189, China.
** Corresponding author.
*** Corresponding author. School of Materials Science and Engineering, Jiangsu Key Laboratory for Advanced Metallic Materials, Southeast University, Nanjing, 211189, China.
E-mail addresses: qwang678@seu.edu.cn (Q. Wang), yt1@ytu.edu.cn (Y. Tong), blshen@seu.edu.cn (B. Shen).

https://doi.org/10.1016/j.msea.2026.149747
Received 27 November 2025; Received in revised form 30 December 2025; Accepted 6 January 2026
Available online 6 January 2026

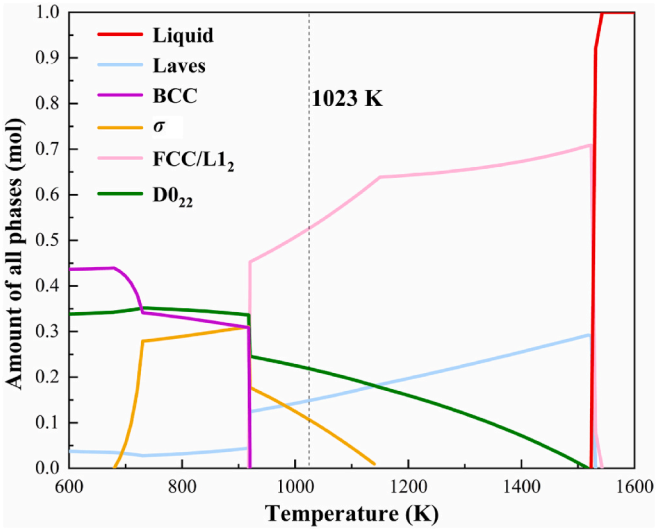

Fig. 1. Thermodynamic phase diagrams of the $CoCrFeNiTa_{0.4}$ EHEA.

Among the various EHEA systems studied, those with FCC-BCC phase configuration have been widely researched. Those EHEAs with moderate mechanical property differences between lamellae often exhibit coordinated deformation between alternating phases, supported by their fine lamellar microstructure and strong interfacial bonding, resulting in an attractive synergy of strength and ductility [4,15–17]. In contrast, FCC-Laves-structured EHEAs with significant mechanical contrast between phases, weak interfaces, and pronounced deformation incompatibility have received considerably less attention. Despite their challenges, such systems offer intriguing opportunities for microstructural turning and property customization. Laves phases have topologically close-packed (TCP) structures with an AB_2 composition [18]. These phases are characterized by high space-filling efficiency, but their inherently limited number of independent slip systems restricts their plastic deformation, resulting in extreme brittleness at room temperature [18,19]. Ojhaa et al. [20] demonstrated that compositionally complexity can mitigate this brittleness. They designed $CoCrFeNi_{2.1}(HfNbTa)_x$ high-entropy alloys (HEAs) containing a Nb-enriched multicomponent Laves phase capable of forming nano-twins. While such a strategy appears promising for FCC-Laves EHEAs, the typical weak interfaces between FCC and Laves lamellae remain a critical concern. Thus, a major challenge lies in designing novel microstructures that simultaneously enhance the interface strength and promote coordinated deformation in FCC-Laves EHEAs.

Inspired by the concept of phase-selective recrystallization [10], we propose a phase-selective transformation strategy involving spatially and structurally targeted $L1_2/D0_{22}$-phase transitions [21,22] to address the weak interface challenge in typical FCC-Laves EHEAs. As reported, multiple phase transformation pathways exist between the FCC, Laves, $L1_2$, and $D0_{22}$ phases, and the favorable lattice matching among these structures often enables the formation of coherent interfaces [22,23]. Additionally, precipitates can exhibit diverse morphologies with distinct shapes and habit planes, while their growth rates are controlled by the anisotropic lattice misfit strains along the *a*- and *c*-axes [24,25]. Therefore, these related characteristics support microstructure tailoring via phase-selective transformation and interface optimization in FCC-Laves EHEAs.

In this study, we developed a novel FCC-Laves-structured EHEA with coherent interfaces by a selective-phase transformation strategy, achieving further enhancement in the strength-plasticity balance. This strategy aims to convert the Laves phase into the $D0_{22}$ phase for constructing a novel eutectic interface, while simultaneously strengthening the FCC lamellae via $L1_2$ nanoprecipitates. It involves two steps: (i) to ensure the occurrences of $L1_2$ and $D0_{22}$ phase-selective transformation. In particular, we chose the Co-Cr-Fe-Ni-Ta high-entropy system because Ta is the formation element of the Laves, $L1_2$, and $D0_{22}$ phases [22,26,27]. The high-entropy effect can promote the formation of multi-principal-element Laves phases. (ii) to tailor phase transition path via aging treatment based on the phase diagram (Fig. 1). For preferential precipitation of $L1_2$ and $D0_{22}$ phases with concurrent suppression of Laves, BCC, and σ phases, the phase transformation pathway was manipulated through 1023 K isothermal aging with precisely controlled duration. During aging, Ta, as a large-atom solute, preferentially segregates to phase boundaries, inducing the nucleation of $D0_{22}$ precipitates. $D0_{22}$ grows via Ta-rich Laves consumption, partially replacing it to form coherent FCC-$D0_{22}$ interfaces. Insufficient Ta within FCC lamellae only yields nanoscale $L1_2$ clusters with coherently embedded interfaces. Thus, the local coherent interfaces are constructed that benefit the mechanical property. Furthermore, the phase transformation and deformation mechanisms were revealed by experimental results and theoretical calculations, including transmission electron microscopy (TEM) characterizations and first-principles calculations. This work provides a new approach to designing coherent heterostructure materials, offering more possibilities for developing strength-plasticity synergized structural alloys.

2. Experimental and calculation methods

2.1. Materials preparation and mechanical tests

Ingots with nominal compositions of $CoCrFeNiTa_{0.4}$ (at.%) were fabricated via vacuum arc melting under an argon atmosphere. Each ingot was remelted at least five times to ensure chemical homogeneity before being suction-cast into a copper mold to produce a cylindrical rod of Φ 3 × 60 mm. The suction-casted rods were isothermally aged at 1023 K for durations of 0.1 h, 1.5 h, 6 h, and 48 h. Hereinafter, the suction-casted and aged EHEAs are denoted as SC, AG-0.1h, AG-1.5h, AG-6h, and AG-48h alloys, respectively. Room-temperature compression tests were performed on cylindrical specimens with dimensions of Φ 3 × 5 mm using an Instron 5982 testing system at a constant strain rate of 10^{-3} s^{-1}. An extensometer was employed for accurate strain measurement. To ensure statistical reliability, three samples were tested for each aging condition.

2.2. Microstructural characterization

The crystal structures of the suction-casted and aged alloys were examined by X-ray diffractometer (XRD, Bruker D8-Discover) with Cu $K\alpha$ radiation, scanned at a rate of 4°/min over a 2θ range from 20 to 80°. Microstructures of the eutectic alloys were analyzed by a field emission scanning electron microscope (SEM, Zeiss Crossbeam350) equipped with electron backscatter diffraction (EBSD) measurements, and a transmission electron microscope (TEM, Thermofisher F200X) equipped with selected area electron (SAED) and energy dispersive spectroscopy (EDS) detectors. Samples for EBSD examination were mechanically polished down to 2 μm with diamond suspension, followed by a vibratory polisher (Buehler Vibromet 2) using nanoscale SiO_2 suspension for 4 h in medium frequency mode. EBSD scans were acquired with a step size of 0.05 μm, and the resulting data were processed using CHANNEL 5 software to determine phase distribution and volume fractions. Samples for TEM analyses were mechanically polished to a thickness of 50 μm using SiC paper and then further thinned by an ion beam thinner (GATAN-M691). High-angle annular dark field (HAADF)-STEM imaging was performed with a collection angle between 72 and 200 m rad. The volume fractions of the $L1_2$ and $D0_{22}$ precipitates were estimated based on TEM images of more than 10 positions. Vickers microhardness of SC and aged alloys was measured using an automatic microhardness tester (FUTURE-TECH FM-700) with a load of 0.98 N and a loading time of 15 s. A 7 × 7 array was indented with an interval of 50 μm on the polished surface of each sample.

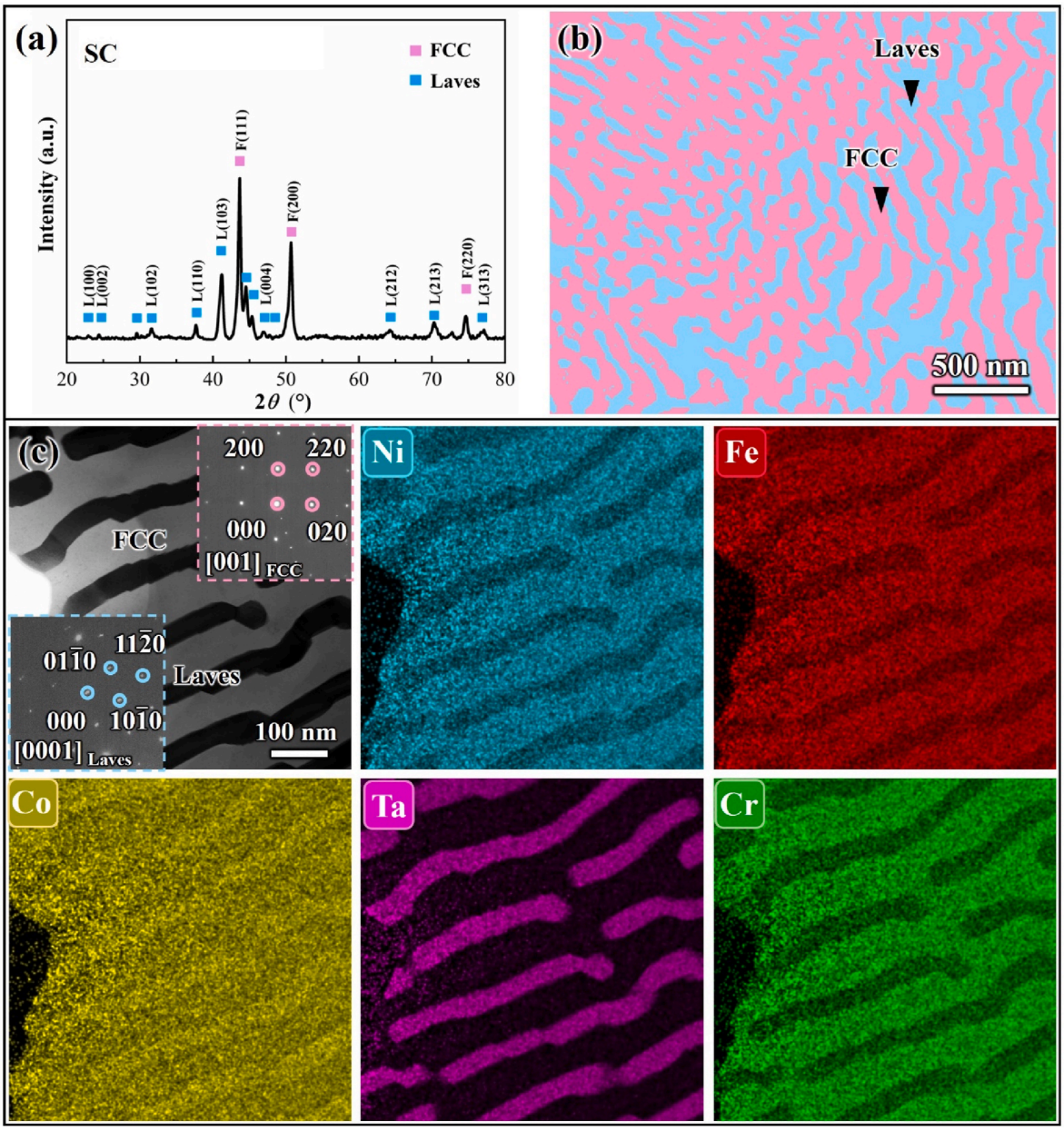

Fig. 2. Microstructure of the suction-casted (SC) alloy. (a) XRD pattern, (b) EBSD phase map. (c) BF TEM image and corresponding elemental distributions.

2.3. Simulation and calculation methods

The phase diagram of the $CoCrFeNiTa_{0.4}$ EHEA was calculated using Thermo-calc software with Nickel base superalloy database [28,29]. The thermodynamic equilibrium phases and transformation pathways were predicted via Gibbs energy minimization under multi-principal component conditions. Additionally, Scheil–Gulliver solidification simulations were conducted to model non-equilibrium microstructural evolution, assuming complete diffusion in the liquid and negligible diffusion in the solid phase.

Based on the density functional theory (DFT), first-principles calculations were performed using the Vienna *ab* initio simulation package (VASP) [30] to investigate the atomic occupation, formation energy, stacking fault energy, and interface relationship of the multiple structures in EHEAs. All calculations were performed using spin-polarized density functional theory to accurately describe the magnetic properties of transition metal elements. The PREDEW-Burke-Ernzerhof (PBE) functional within the generalized gradient approximation (GGA) [31] was adopted to describe exchange-correlation interactions [32]. The projector augmented-wave (PAW) [33] method was employed to model ion-electron interactions. Structural relaxations were performed until the Hellmann-Feynman forces on all atoms were less than 0.05 eV/Å and the energy convergence criterion reached 10^{-6} eV.

Modeling random alloys presents a challenge within periodic boundary conditions, as finite supercell sizes may introduce artificial correlations. To better approximate chemical randomness, special quasi-random structures (SQS) were employed. For consistent comparison of formation energies and interfacial properties, periodic 32-atom cells for the $L1_2$, $D0_{22}$, and σ structures and 40-atom supercells for the FCC and Laves structures were constructed. Calculations of the total energy for each cell were performed with a plane-wave cutoff energy of 400 eV and a Monkhorst-Pack k-point mesh, where a grid density corresponding to 0.04 $Å^{-1}$ was used [32].

To identify the most suitable interfaces for calculation, we selected the two with the lowest misfit degree, based on computed interface energies and misfit degrees for all low-index FCC-$L1_2$ and FCC-$D0_{22}$

Table 1
Element compositions of FCC, Laves, $L1_2$, and $D0_{22}$ phases in EHEAs.

Sample	phase	Element content (at. %)				
		Co	Cr	Fe	Ni	Ta
Nominal	Nominal	22.7	22.7	22.7	22.7	9.2
Suction-cast	FCC	22.01 ± 0.87	25.56 ± 0.88	26.43 ± 0.66	23.17 ± 0.79	2.83 ± 2.00
	Laves	23.94 ± 0.30	16.94 ± 0.30	19.29 ± 0.15	17.84 ± 0.28	21.99 ± 0.05
AG-0.1h	FCC	21.29 ± 3.28	23.93 ± 2.74	23.68 ± 2.85	27.59 ± 2.64	3.51 ± 3.35
	Laves	24.58 ± 1.16	16.00 ± 1.49	20.24 ± 1.30	17.66 ± 1.60	21.52 ± 0.79
	cuboidal $L1_2$	27.06 ± 5.60	19.26 ± 7.29	17.58 ± 7.29	26.97 ± 5.91	9.13 ± 4.11
	$D0_{22}$	14.26 ± 4.46	4.13 ± 6.78	8.87 ± 4.32	47.41 ± 1.62	25.33 ± 2.11
AG-6h	FCC	22.61 ± 1.39	25.65 ± 0.84	28.13 ± 0.99	20.65 ± 1.24	2.96 ± 2.12
	Laves	28.17 ± 3.37	21.69 ± 4.40	24.69 ± 4.39	7.61 ± 6.99	17.84 ± 3.56
	cuboidal $L1_2$	28.05 ± 9.23	14.90 ± 5.88	21.29 ± 4.32	24.55 ± 6.95	11.21 ± 6.16
	$D0_{22}$	23.60 ± 1.41	5.87 ± 6.54	5.99 ± 4.32	45.35 ± 0.92	19.19 ± 1.18
	σ	20.19 ± 2.76	28.79 ± 2.68	23.97 ± 3.10	22.57 ± 2.56	4.48 ± 3.59
AG-48h (all $L1_2$ precipitates from the anomalous eutectic zone)	FCC	21.65 ± 0.89	25.96 ± 0.71	29.70 ± 0.86	20.56 ± 1.04	2.13 ± 3.92
	Laves	29.47 ± 2.51	15.94 ± 3.70	26.55 ± 2.53	8.77 ± 7.24	19.27 ± 2.12
	cuboidal $L1_2$	25.88 ± 8.99	9.39 ± 4.21	17.95 ± 9.36	28.55 ± 7.07	18.23 ± 8.94
	needle-like $L1_2$	21.89 ± 9.48	2.67 ± 5.60	3.10 ± 6.83	47.14 ± 5.52	25.20 ± 6.27
	$D0_{22}$	25.62 ± 0.37	5.85 ± 0.91	8.60 ± 1.03	41.81 ± 0.23	18.12 ± 0.25
	σ	16.60 ± 0.48	50.47 ± 0.19	25.16 ± 0.43	6.65 ± 0.72	1.12 ± 2.03

surfaces. A series of tests was performed to ensure the suitable atomic layers for the FCC, Laves, and $D0_{22}$ slabs that the slabs met the bulk-like interiors. The FCC-Laves interface is modelled by stacking a four-layer $(1120)_{Laves}$ slab onto a two-layer $(100)_{FCC}$ slab, while the FCC-$D0_{22}$ interface consists of a five-layer $(100)_{FCC}$ slab onto a ten-layer $(100)_{D022}$ slab. Then, structure optimization is carried out in the unit cell structure of both interfaces. A vacuum layer of 15 Å was applied to eliminate spurious interactions between periodic image slabs [34,35]. The k-point mesh was generated using the Monkhorst-Pack scheme with a grid density corresponding to a resolution of 0.04 $Å^{-1}$. Energy and stress convergence thresholds were set to 2×10^{-5} eV/atom and 0.05 eV/Å.

For stacking fault energy calculations in FCC and Laves phases, a 108-atom SQS supercell was built with periodic boundaries along the (111) plane. A vacuum region of 15 Å was added normal to the surface, and a stacking fault was generated by rigidly shifting the upper four [111] atomic layers along the [112] direction. The stacking sequence was systematically modified to ensure the fault was centered within the supercell. The Brillouin zone (BZ) was sampled using a Gamma-point-based 4 × 4 × 2 k-point mesh. The Methfessel-Paxton smearing method with a width of 0.1 eV was applied for k-space integration over the BZ [36]. During SFE calculations, atomic positions were relaxed along the close-packed direction until forces were below 10^{-2} eV/Å, while lattice parameters remained fixed.

3. Results

3.1. Microstructure of suction-casted alloy

The suction-cast (SC) alloy exhibits a dual-phase structure consisting of FCC and Laves phases, as identified by the XRD spectrum in Fig. 2a. A representative EBSD map in Fig. 2b reveals an alternate lamellar morphology, illustrating the formation of FCC-Laves eutectic structure. The average lamellar width of the FCC and Laves phases is 86.7 ± 3.4 nm and 47.2 ± 4.9 nm, respectively, and their relative volume fractions

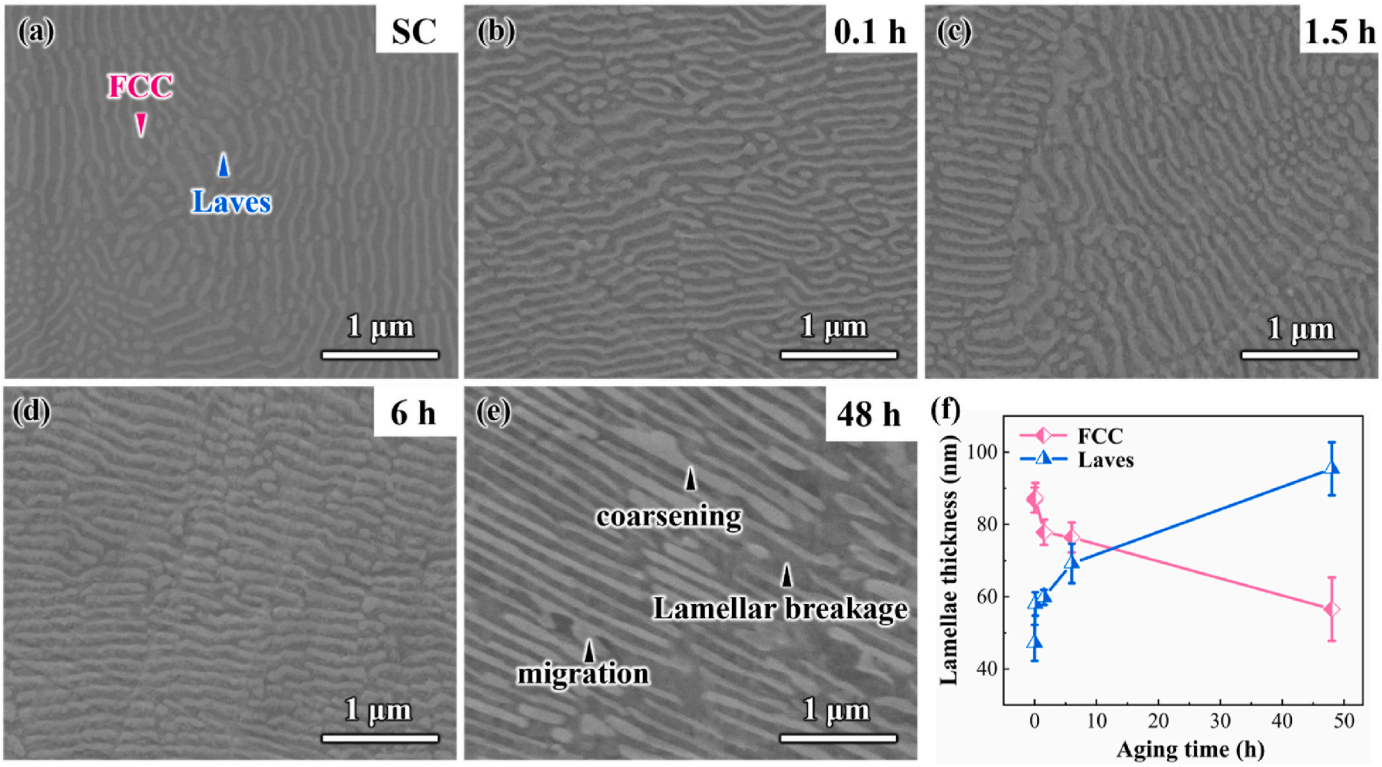

Fig. 3. Lamellar width of the suction-casted and subsequently aged alloys. SEM images of (a) SC, (b) AG-0.1h, (c) AG-1.5h, (d) AG-6h, and (e) AG-48h alloys. (f) Summarized lamellar widths of these alloys.

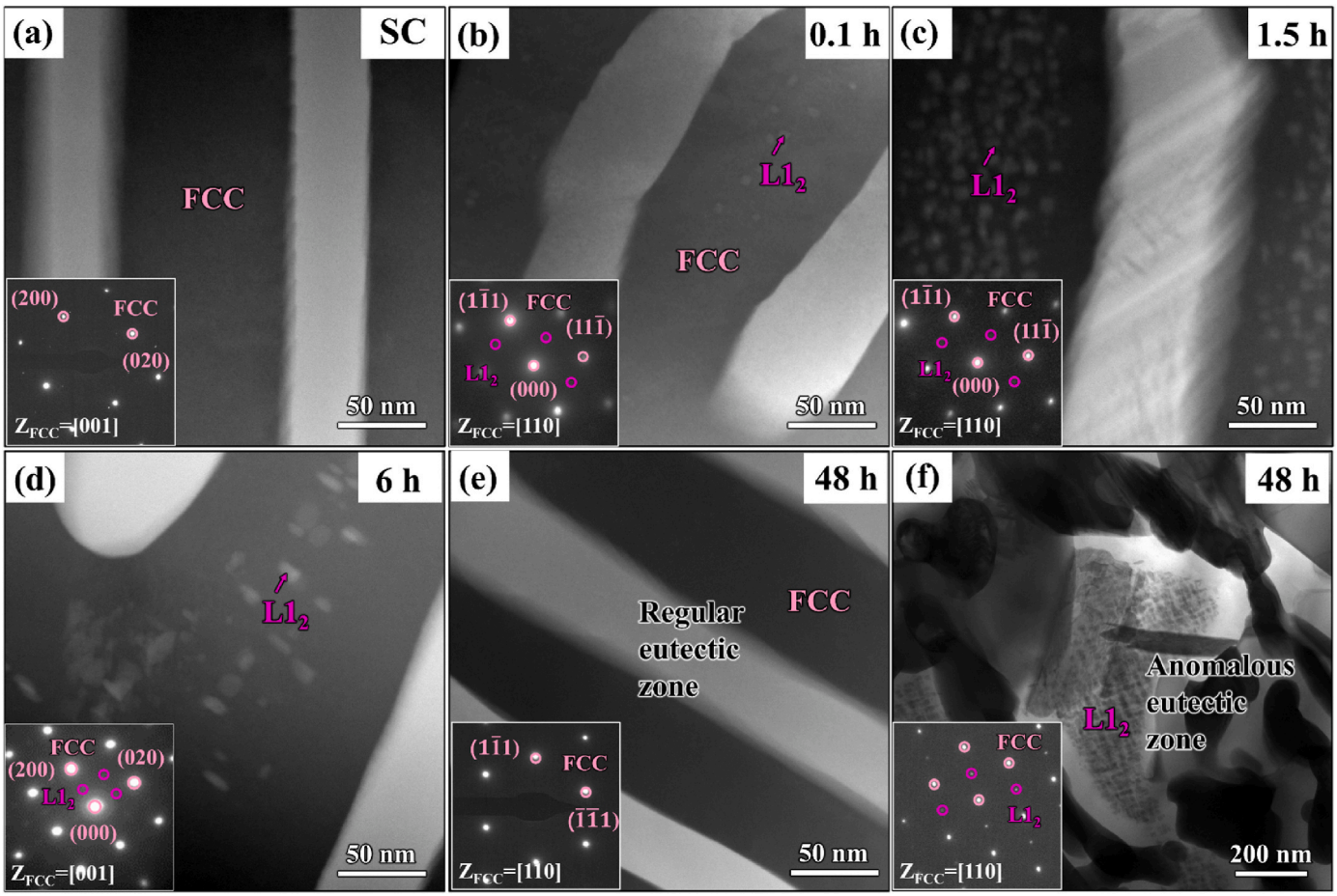

Fig. 4. Phase transformation within the FCC lamellae in the suction-casted and aged alloys. HAADF images the corresponding SAED patterns of (a) SC, (b) AG-0.1h, (c) AG-1.5h, (d) AG-6h, and (e–f) AG-48h alloys.

are 68 % and 32 %. Besides, the bright-field (BF) TEM image with SAED patterns in the insets further confirms the alternating FCC and Laves assemblies (Fig. 2c) and their nanoscale thickness. Elemental distribution mappings (Fig. 2c) for Co, Cr, Fe, Ni, and Ta were acquired via STEM-EDS. Their compositions are summarized in Table 1. The FCC lamellae are enriched in Cr, Fe, and Ni, with measured compositions of 22.01 ± 0.87 % Co, 25.56 ± 0.88 % Cr, 26.43 ± 0.66 % Fe, 23.17 ± 0.79 % Ni, together with a small amount of Ta (2.83 ± 2.00 %), whereas the Laves phase contains higher concentrations of Co and Ta, with compositions of 23.94 ± 0.30 % Co, 16.94 ± 0.30 % Cr, 19.29 ± 0.15 % Fe, 17.84 ± 0.28 % Ni, and 21.99 ± 0.05 % Ta. It is evident that Cr, Fe, and Ni partition primarily to the FCC lamellae, whereas Co and Ta preferentially partition to the Laves lamellae. The atomic ratio of (Ta + Fe) to (Ni + Cr + Co) in the Laves phase is around 1:2, consistent with the crystal chemical formula (Ta, Fe)(Ni, Cr, Co)$_2$.

3.2. *Phase-selective transformation after aging*

Fig. 3 shows the backscattered electron (BSE) images of the alloys in both suction-cast condition and after isothermal aging at 1023 K for various durations. The typical FCC-Laves lamellar microstructure remains stable after aging for up to 6 h (Fig. 3b–d). However, upon extended aging for 48 h, significant microstructural evolution occurs, including migration, coarsening, and fragmentation of the Laves lamellae (Fig. 3e). These changes result in an increase in the average width of the Laves lamellae, and a corresponding reduction in that of the FCC lamellae (Fig. 3f). The measured areal fractions of the FCC and Laves phases in AG-48h alloy are approximately 60 % and 40 %, respectively. To further investigate these evolutionary behaviors within the FCC and Laves lamellae, detailed TEM analyses are conducted.

3.2.1. *$L1_2$-phase-selective transformation behavior within the FCC lamellae*

HAADF-STEM was performed to investigate the microstructural evolution within the FCC lamellae in the suction-cast and aged alloys (Fig. 4). In the suction-cast condition, only FCC diffraction spots are detected (Fig. 4a). After isothermal aging, cuboidal precipitates become evident in the HADDF-STEM images of the FCC lamellae. The accompanying SAED patterns, acquired along the [110] or [001] zone axes, reveal the presence of $L1_2$-type superlattice spots (Fig. 4b–d). The volume fraction of the $L1_2$ phase increases initially with aging time, reaching a maximum in AG-1.5h alloy, and subsequently decreases. Upon aging for 48 h, the $L1_2$ precipitates are no longer observed within the regular FCC lamellae (Fig. 4e), whereas both cuboidal and needle-like $L1_2$ morphologies gather within limited anomalous eutectic zone (Fig. 4f). Further investigation using high-resolution TEM (HRTEM) reveals the ordering transition process of the $L1_2$ within the FCC lamellae (Fig. 5). While $L1_2$ ordered domains are scarcely detectable in SC alloy, their size approaches 15 nm after 6 h aging. Continuous lattice fringes with no discernible misorientation in the HRTEM images indicate that the $L1_2$ precipitate maintains coherence with the FCC matrix. Integrated intensity profiles derived from fast Fourier transform (FFT) patterns (Fig. 5a–d) demonstrate a notable increase in the intensity of superlattice spots in AG-6h alloy, compared to the suction-cast condition.

EDS analysis reveals preferential partitioning of Ni, Ta, and Co to $L1_2$ precipitates while Cr and Fe are enriched in the FCC matrix (Fig. 6a and b). The cuboidal $L1_2$ particle exhibits a time-dependent coarsening behavior, with the composition evolving from $Co_{27}Cr_{19}Fe_{18}Ni_{27}Ta_9$

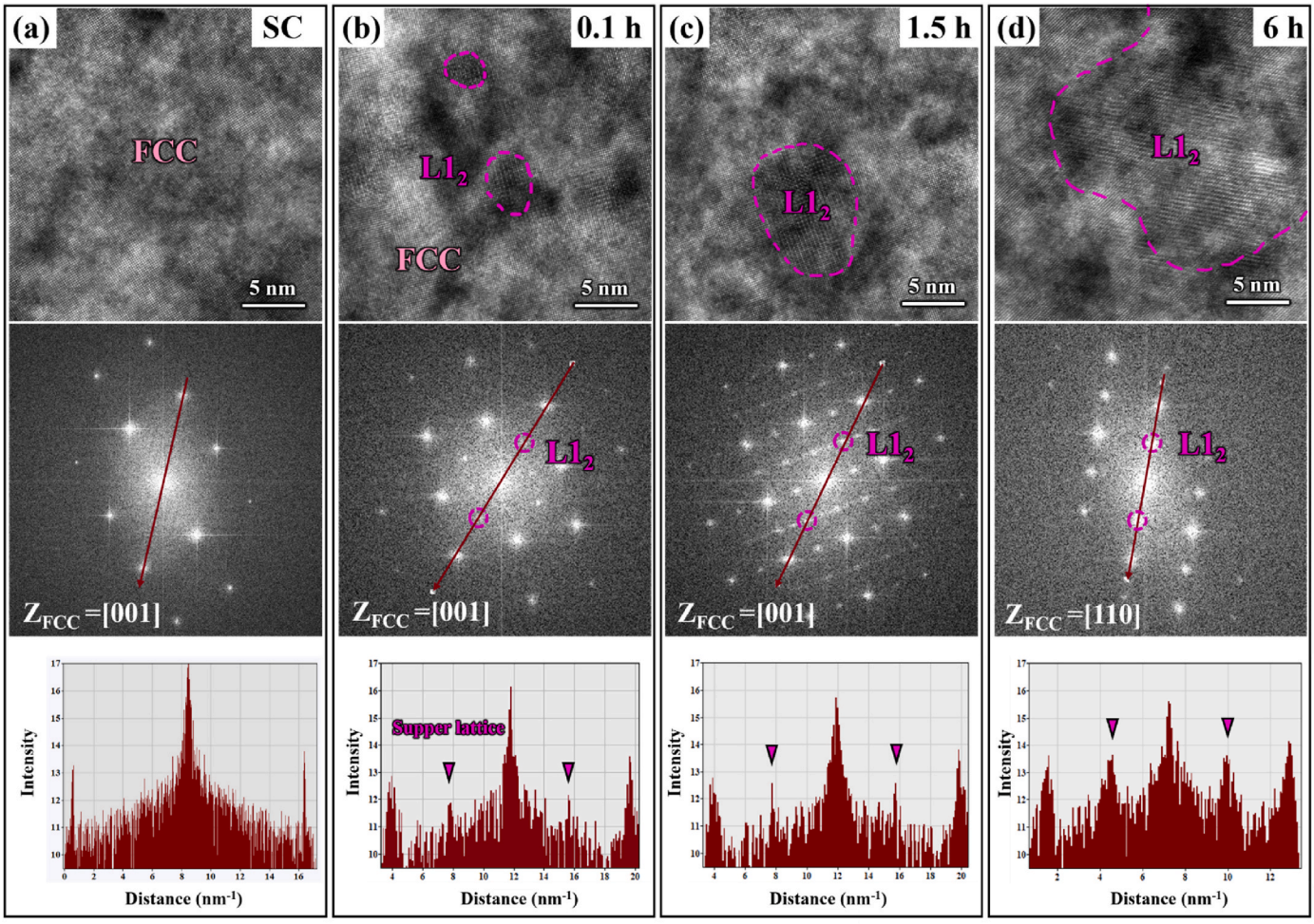

Fig. 5. Structure of L12 precipitates in the FCC lamellae. HRTEM images, SAED patterns, and the intensity profiles along the red arrows for the (a) SC, (b) AG-0.1h, (c) AG-1.5h, and (d) AG-48h alloys. (For interpretation of the references to colour in this figure legend, the reader is referred to the Web version of this article.)

(AG-0.1h alloy, Fig. 6c) to $Co_{26}Cr_9Fe_{19}Ni_{28}Ta_{18}$ (AG-48h alloy, Fig. 6d). Meanwhile, the needle-like $L1_2$ phase in AG-48h alloy (Fig. 6e) shows even higher concentration of Ni, Ta, and Co, accompanied by reduced Fe and Cr. This progression is chemically driven by uphill diffusion [37], with average Ni and Ta concentrations increasing from 26.97 ± 5.91 % and 9.13 ± 4.11 % at 0.1 h to 47.14 ± 5.52 % and 25.20 ± 6.27 % in AG-48h alloy (Table 1). The formation of $L1_2$ precipitation in AG-48h alloy requires higher Ni and Ta concentrations. However, the content of Ta element in regular FCC lamellae is only 3 %, a composition insufficient to support uphill diffusion. And no $L1_2$ precipitates form within the regular lamellar zones of the AG-48h alloy, not even the cuboidal variant. Additionally, $L1_2$ depletion zones exist near the interface (Fig. 6f), attributed to the preferential partitioning of Ta into the Laves lamellae.

3.2.2. DO_{22}-phase-selective transformation behavior within the Laves lamellae

BF TEM images in Fig. 7 illustrate the microstructural evolution of the Laves lamellae following isothermal aging. In the suction-cast condition, the Laves phase exhibit a homogeneous elemental distribution without detectable precipitates (Fig. 2c). After aging, however, a distinct phase transformation is observed, evidenced by the appearance of $D0_{22}$-type superlattice reflections in selected area electron diffraction (SAED) patterns (Fig. 7a). The extent of this transformation increases with aging time (Fig. 7b–d), with the $D0_{22}$ phase accounting for over 50 % of the originally Laves-dominated regions after 6 h, accompanied by a corresponding reduction in the Laves fraction.

Further TEM analysis reveals that incipient σ phase nucleates in the Ni-Ta-enriched $D0_{22}$ structure (Fig. 8a) beginning in AG-6h alloy, which can be specifically determined as FeCr stoichiometry by the EDS maps (Fig. 8b). An HRTEM image in Fig. 8c captures the structural transition region between the $D0_{22}$ and σ phases. A high density of stacking faults (SFs) was formed in the $D0_{22}$ phase. To further elucidate the atomic structure of the σ phase, atomic-scale analysis was performed on a coarsened Fe-Cr-rich particle in AG-48h alloy (Fig. 8d). The HRTEM image in Fig. 8e reveals chemically ordered domains, and the FFT pattern confirms an orthorhombic structure. An inverse FFT (IFFT) image reconstructed along the [100] axis (Fig. 8f) clearly resolves an orthogonal atomic arrangement wherein Fe and Cr occupy distinct sublattice sites, as illustrated in the schematic inset. The measured interatomic spacing between adjacent Fe-Fe and Cr-Cr columns is approximately 0.247 nm. Note that the apparent coarsening of Laves lamellae observed via SEM (Fig. 3e) can be attributed to these phase transformations, but it remains challenging to clarify nanoscale transitions due to the limited imaging resolution.

$L1_2/D0_{22}$ phase-selective transformation of the eutectic lamellae is anticipated to induce significant changes in the interfacial relationships, as illustrated by the HRTEM analysis of the interfacial characteristics in AG-6h alloy (Fig. 9). Based on the Bramfitt lattice matching theory [38], the mismatching degree factors ($\overline{\delta^{(hkl)_s}_{(hkl)_n}}$) between the original FCC-Laves lamellae and post-transformational FCC-$D0_{22}$ lamellae are calculated

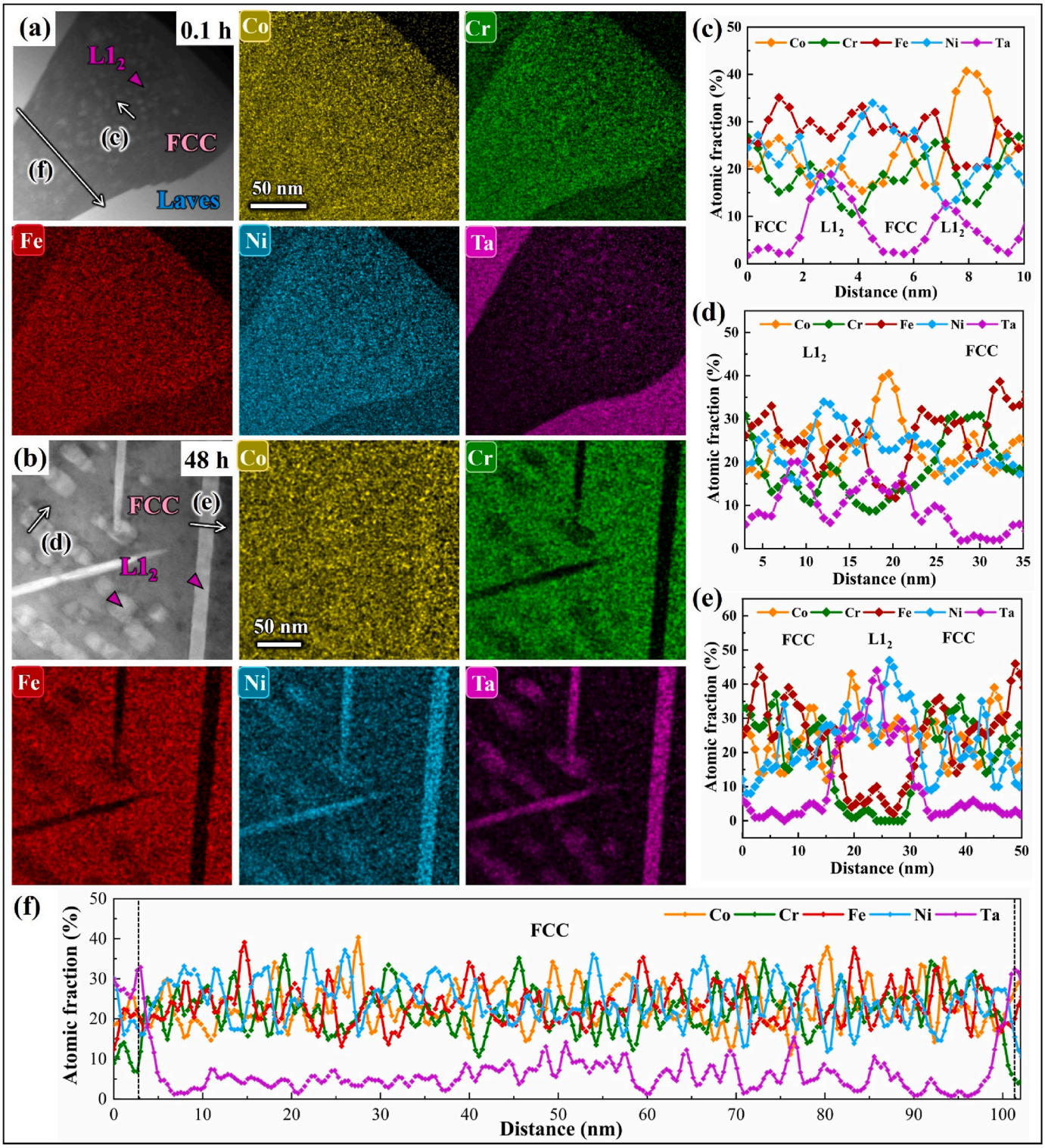

Fig. 6. Element composition of L12 precipitates in the FCC lamellae. Elemental mappings of (a) AG-0.1h, (b) AG-48h alloys. Projected one-dimensional concentration profiles along white arrows in (a) and (b) are shown in (c–f).

$$\overline{\delta^{(hkl)_s}_{(hkl)_n}} = \sum_{i=1}^{3} \frac{\left| d_{[uvw]^i_s} \cos\theta - d_{[uvw]^i_n} \right|}{d_{[uvw]^i_n}} \times 100\% \quad (1)$$

where $(hkl)_s$ and $(hkl)_n$ are miller indices for the crystal planes of two phases, $[uvw]_s$ and $[uvw]_n$ are miller indices for the crystal directions on $(hkl)_s$ and $(hkl)_n$ planes, respectively, $d_{[uvw]s}$ and $d_{[uvw]n}$ are the interatomic spacing along $[uvw]_s$ and $[uvw]_n$, which are derived from the lattice parameters measured by TEM, θ is the included angle between two crystal planes, and its value is marked in the pictures (Fig. 9b–e). Experimentally determined interface orientations are $(\bar{2}\ 00)_{FCC}//(\bar{2}3\bar{1}0)_{Laves}$, $[011]_{FCC}//[0001]_{Laves}$ and $(\bar{1}1\bar{1})_{FCC}//(004)_{Laves}$, $[011]_{FCC}//[10\ \bar{4}]_{Laves}$. The calculated mismatch degree factors of these FCC-Laves and FCC-$D0_{22}$ interfaces are 14.27 % and 5.53 %,

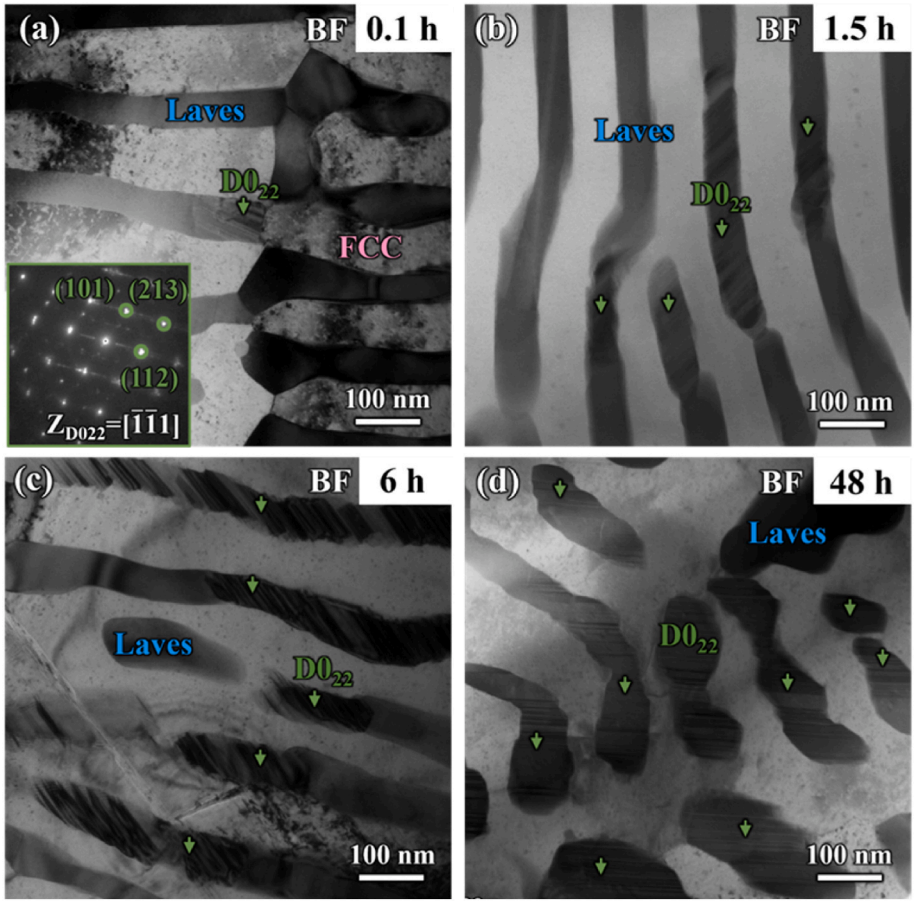

Fig. 7. Phase transformation of the Laves lamellae in the aged alloys. BF images of the $D0_{22}$ precipitates in (a) AG-0.1h alloy, inset: corresponding SAED patterns of $D0_{22}$ structure, (b) AG-1.5h, (c) AG-6h, and (d) AG-48h alloys.

respectively. The misfit at the semi-coherent interface decreases after $D0_{22}$ phase transformation, evolving toward a coherent bonding, as evidenced by the interfacial structure revealed in the HRTEM images (Fig. 9b–d) and further IFFT images (Fig. 9c–f).

3.3. Mechanical properties

Fig. 10a displays the engineering stress-strain curves of the EHEAs under uniaxial compression as a function of aging time. The yield strength and microhardness of the alloys initially increase with aging time, reaching a maximum value at 2308 MPa and 645 HV in AG-1.5h alloy, followed by a slightly decline upon further aging (Fig. 10b). The compressive strain decreases slightly in AG-0.1h alloy, then it increases continuously with extended aging time, culminating in a maximum in AG-48h alloy (Fig. 10c). Overall, the AG-6h alloy shows an optimal balance of strength and compressive strain with values of 2986 MPa and 12 %, respectively, where the compressive strain is approximately double that of the SC alloy. A comparison of compressive strength and strain between the present FCC-Laves EHEAs with the reported single-phase Laves alloys and dual-phase Laves alloys is summarized in Fig. 10d. The AG-6h EHEA exhibits a good balance of compressive strength-plasticity property.

4. Discussion

4.1. Mechanisms of phase-selective transformation

TEM results reveal that the aging treatment induces phase-selective transformation, wherein the soft FCC phase evolves an $L1_2$-ordered intermetallic precipitates, while the Laves lamellae develop deformable $D0_{22}$ and σ phases. To explore the thermodynamic origin of these aging-induced selective transformations of $L1_2$, $D0_{22}$, and σ phases, we calculated and compared their formation energies using first-principles calculations. Based on the chemical analysis summarized in Table 1, the $L1_2$ and $D0_{22}$ precipitates adopt a Ni_3Ta-type configuration, with Ta atoms occupying the corner sites of the cell [22]. When the Ta content is lower than 25 at.%, Fe or Cr atoms may partially occupy the Ta sublattice [39,40], which can influence the relative stability of $L1_2$ and $D0_{22}$ structures. Here, first-principles calculations were performed in 32-atom supercells with compositions scaled according to Table 1. The formation energy per atom was evaluated using the equation from Scott [41]:

$$\Delta E^{formation} = \frac{E^{total} - A \times \mu_a - (B-A) \times \mu_b}{B} \quad (2)$$

where E^{total} represents the total energy of the supercell, μ_a and μ_b denote the chemical potentials of the pure substitution atoms computed by presuming the identical cell symmetry, respectively. A is the number of substituted atoms, and B is the total number of atoms in the system.

Three $L1_2$-ordered models are constructed, as shown in Fig. 11. Model 1 is based on the Ni_3Ta composition. Model 2 corresponds to the $(Co_{28}Ni_{25}Fe_{14}Cr_8)(Ta_{11}Cr_7Fe_7)$ composition with 14 at.% Cr and Fe occupying the Ta sublattice, which proportionally scaled down to $(Co_9Ni_8Fe_5Cr_2)(Ta_3Cr_2Fe_3)$ to represent the $L1_2$ phase in AG-6h alloy. Model 3 is derived from the $(Co_{22}Ni_{47}Fe_3Cr_3)(Ta_{25})$ composition and proportionally scaled down to $(Co_7Ni_{15}Fe_1Cr_1)(Ta_8)$, corresponding to the needle-like $L1_2$ precipitates formed in the anomalous eutectic region in AG-48h alloy. The results indicate that model 3 has the lowest formation energy, confirming that the needle-like $L1_2$ phase is the most

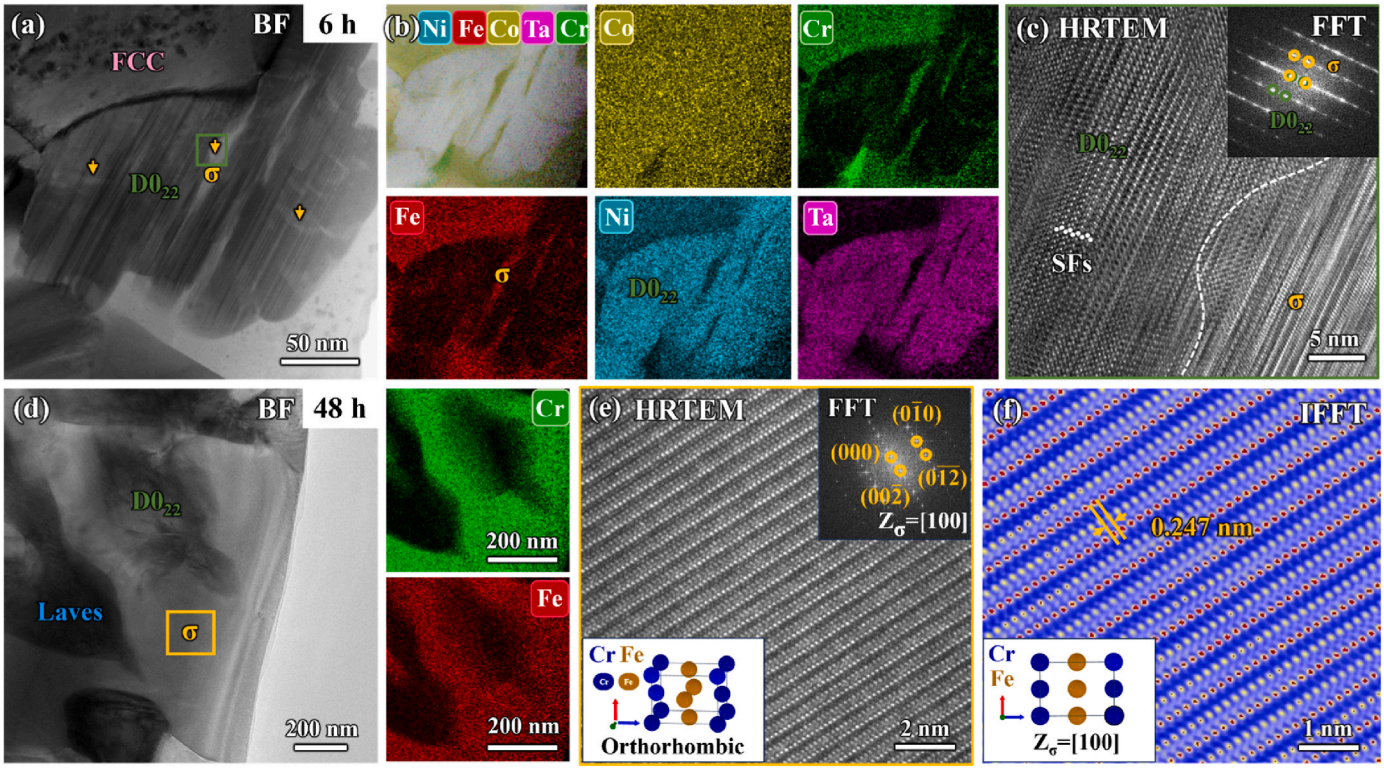

Fig. 8. Phase transformation of the Laves lamellae in the aged alloys. AG-6h alloy: (a) BF image shows an initial σ-phase nucleation in the $D0_{22}$ structure. (b) EDS mapping to reveal the elemental partition within the $D0_{22}$ and σ transformation region. (c) HRTEM image of the area highlighted by the green box in (a) shows a high density of SF in the $D0_{22}$ and σ structure. **AG-48h alloy:** (d) BF image exhibits the coarsened σ phase that is rich in Cr and Fe. (e–f) HRTEM, FFT patterns, and inverse FFT image of σ phase. Inset: the unit cell structure of FeCr-type σ phase, with orthorhombic symmetry. (For interpretation of the references to colour in this figure legend, the reader is referred to the Web version of this article.)

thermodynamically stable. The higher Ta content in this model leads to a more negative formation energy, favoring $L1_2$ precipitation under prolonged aging. However, the limited Ta solubility (~3 at.%) in the FCC lamellae hinders the enrichment necessary to reach ~25 at.% Ta through diffusion, thereby inhibiting $L1_2$ precipitation within regular eutectic domains. According to the cubic $L1_2$ detected in regular eutectic domains in AG-6h alloy (Table 1), uphill diffusion enables Ta enrichment only up to ~11 at.%.

Within the Laves lamellae, aging promotes the coprecipitation of nanoscale $D0_{22}$ and σ phases. We calculated the formation energies of theses phases in AG-6h alloy (Fig. 11). Model 4 is based on the $D0_{22}$ phase with a Ni_3Ta-type configuration, while Model 5 and Model 6 represent the $D0_{22}$ phase with $(Ni_{46}Co_{24}Cr_2Fe_3)(Ta_{19}Cr_3Fe_3)$ composition and the σ phase with $(Cr_{29}Fe_{17}Ta_4)(Co_{20}Fe_7Ni_{23})$ composition, which are proportionally scaled down as $(Ni_{14}Co_8Cr_1Fe_1)(Ta_6Cr_1Fe_1)$ and $(Cr_9Fe_6Ta_1)(Co_6Fe_2Ni_8)$, respectively. The formation energy of the σ phase is significantly lower than that of the Ni_3Ta-type $D0_{22}$ structure (model 4), suggesting that the coprecipitation of $D0_{22}$ and σ phases constitutes a more stable configuration. The lattice parameters of the Laves are $a = 0.479$ nm and $c = 0.782$ nm [42], while those for the tetragonal $D0_{22}$ phase are $a = 0.366$ nm and $c = 0.748$ nm [43]. The morphology of the coherent $D0_{22}$ precipitate is controlled by anisotropic coherency strain fields, which originate from the tetragonality-induced lattice mismatch with the Laves lamellae (along the a- and c-axes) [24,25]. Takeyama et al. [44] reported that in Ni-Nb alloys, an increased misfit along the preferred growth direction retards the growth kinetics of the coherent Ni_3Nb-$D0_a$ phase within the Al matrix. This inverse relationship implies that the smaller the misfit directly promotes the faster the growth. In the present study, the multi-principal element $D0_{22}$ precipitate exhibits a lath shape due to its anisotropic kinetics, with preferential advancement along the c-axis over the a-axis. This growth characteristic leads to alignment and propagation along the pre-existing Laves lamellae, resulting in their partial replacement, while the resultant $D0_{22}$ precipitates retain coherent interfaces with the surrounding FCC matrix. Additionally, the Fe-Cr-enriched σ precipitates are observed to coprecipitate with the $D0_{22}$ phases, suggesting a strong correlation in their formations [45]. While the Laves lamellae initially exhibit a near-equilibrium elemental distribution across all constituent elements (Fig. 2c), Co preferentially partitions into the $D0_{22}$ domains upon the formation of Ni-Ta-enriched $D0_{22}$ precipitates due to its strong affinity for Ni/Ta coordination, while Cr and Fe are repelled (Fig. 8b). Sustained thermal-activated diffusion creates a Cr-Fe-rich environment conductive to σ phase precipitations [40]. This phase-selective transformation in both the FCC and Laves lamellae contributes to the reduced interface misfit and cooperative deformation of the hierarchical heterostructure.

4.2. *Interfacial restructuring during phase transformation*

Based on Fig. 9, the $D0_{22}$-phase-selective transformation facilitates the conversion of some FCC-Laves interfaces into FCC-$D0_{22}$ interfaces, thereby reducing interfacial misfit. To assess the generality of this phenomenon, low-index interface models, specifically $(100)_{FCC}/(1120)_{Laves}$ and $(100)_{FCC}/(100)_{D022}$-were constructed and analyzed based on the first-principles calculations (Fig. 12). The calculated lattice misfits were 17.7 % for the FCC-Laves interface and 1.4 % for the FCC-$D0_{22}$ interface, indicating that phase-transformation-induced interfacial restructuring enhances the bonding coherence across eutectic lamellae.

Interfacial energy (γ_{int}), referring to the energy required to form an interface from two separated surfaces, serves as an indicator of bonding strength and interfacial stability [46,47]. Typically, a lower interfacial energy corresponds to stronger bonding and enhanced stability [48]. The interfacial energy was evaluated using the following expression [49,

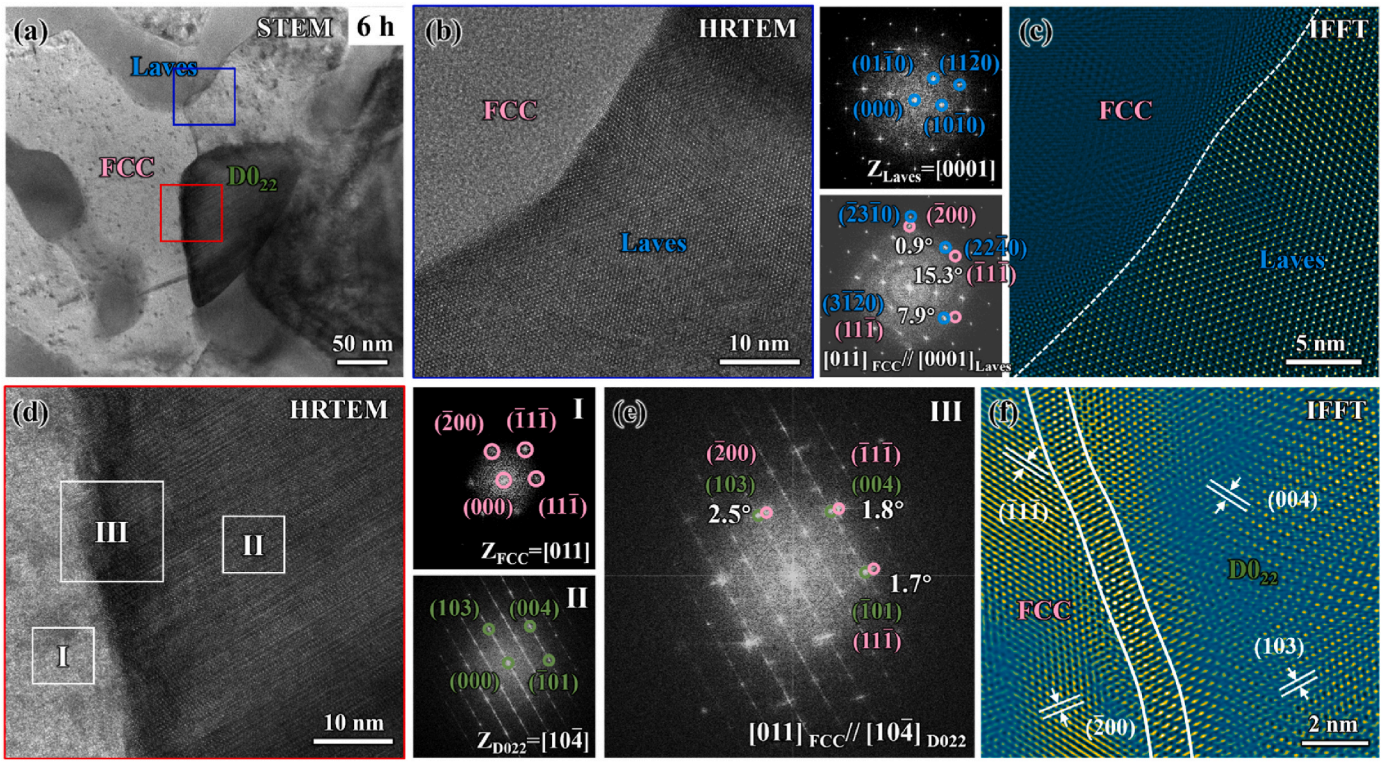

Fig. 9. Interfacial orientation relationship in the AG-6h alloy. (a) STEM image with $D0_{22}$ transition. (b–c) Enlarged HRTEM image of the blue box in (a), corresponding FFT patterns, and interfacial IFFT image of original FCC-Laves eutectic lamellae. (d–f) Enlarged HRTEM image of the red box in (a), corresponding FFT patterns, and interfacial IFFT image of post-transformation FCC-$D0_{22}$ eutectic lamellae. (For interpretation of the references to colour in this figure legend, the reader is referred to the Web version of this article.)

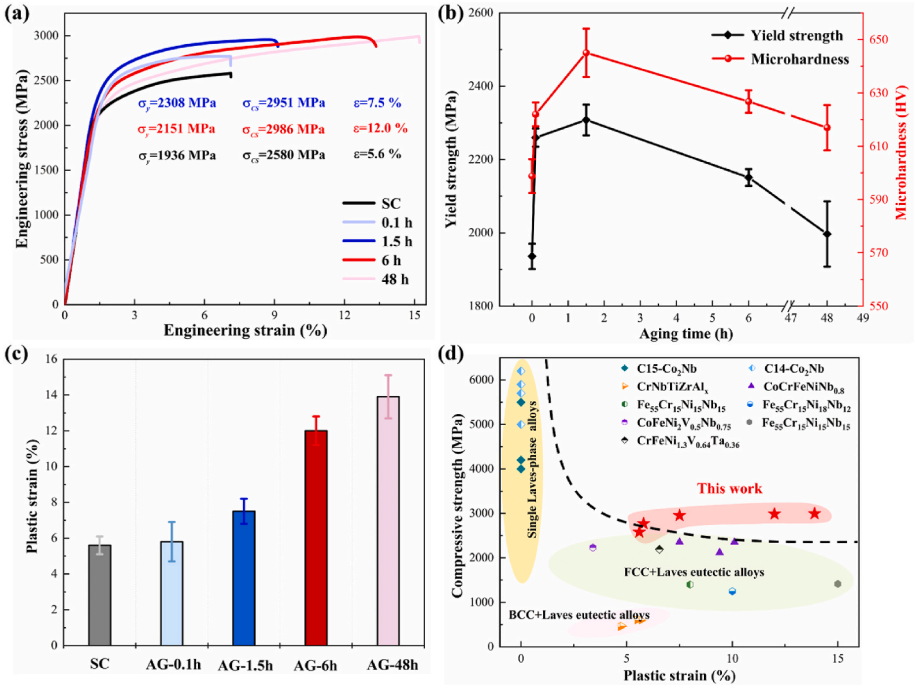

Fig. 10. Mechanical properties of the suction-casted and aging alloys. (a) The engineering stress-strain curves at room temperature, (b) the plastic strain, (c) the yield strength and microhardness values, and (d) a good balance of strength and plasticity of current FCC-Laves EHEAs compared with single Laves-phase alloys [64] and Laves-dual phase alloys [65–70].

50]:

$$\gamma_{int} = \left(E_{total}\text{-}E_{surface1}\text{-}E_{surface2}\right) / A \quad (3)$$

where E_{total} is the total energy of an interface supercell corrected for free surfaces, $E_{surface1}$ and $E_{surface2}$ are the energies of the isolated FCC and

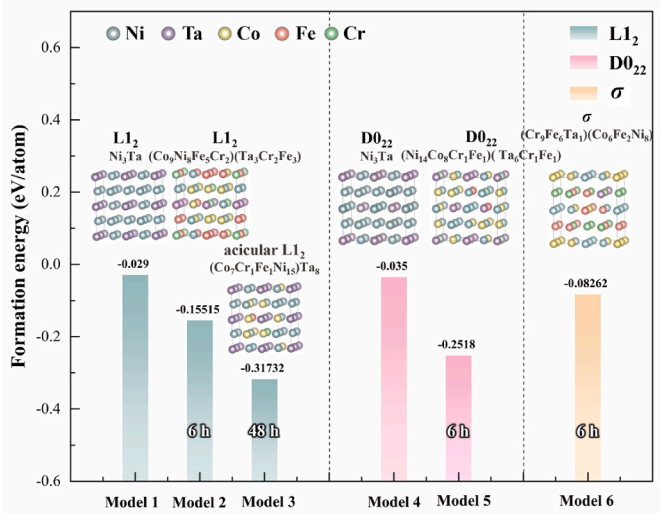

Fig. 11. Formation energies of L12/D022-Ni3Ta structure with various compositions and σ-CrFe phase. Model 1–3 show the formation energies of A_3B-type $L1_2$ structures with Ni_3Ta, $(Co_9Ni_8Fe_5Cr_2)(Ta_3Cr_2Fe_3)$ [$(Co_{28}Ni_{25}Fe_{14}Cr_8)(Ta_{11}Cr_7Fe_7)$] in AG-6h alloy and $(Co_7Cr_1Fe_1Ni_{15})(Ta_8)$ [$(Co_{28}Cr_3Fe_7Ni_{33}Ta_4)(Ta_{25})$] in AG-48h alloy. Model 4 and 5 present the formation energies of A_3B-type $D0_{22}$ structures with Ni_3Ta and $(Ni_{14}Co_8Cr_1Fe_1)(Ta_6Cr_1Fe_1)$ [$(Ni_{46}Co_{24}Cr_2Fe_3)(Ta_{19}Cr_3Fe_3)$] in AG-6h alloy. Model 6 presents the formation energy of the σ phase in the AG-6h alloy.

Laves/$D0_{22}$ surfaces, respectively, and A is the interfacial area. The calculated interfacial energies are 1.64 J/m^2 for FCC/Laves and 0.12 J/m^2 for FCC/$D0_{22}$. Obviously, the $D0_{22}$ phase-selective transformation substantially reduces the FCC-$D0_{22}$ interfacial energy, enhancing stability and bonding strength [48]. Studies have reported that the high interfacial energy (e.g., 3.58 J/m^2 at the low-index TiC-Fe interface) corresponds to intrinsically weak bonding and serves as a failure-prone site in the metal-ceramic composite [35]. Similarly, in FCC-Laves EHEAs, the substantial lattice misfit (measured experimentally as 14.27 % for $(\bar{1}1\bar{1})_{FCC}//(\bar{2}3\bar{1}0)_{Laves}$ with $[011]_{FCC}//[0001]_{Laves}$, and computed as 17.7 % for $(100)_{FCC}//(1120)_{Laves}$ with $[010]_{FCC}//[0001]_{Laves}$, and high interfacial energy (1.64 J/m^2) leads to semi-coherent interfaces with inherently limited bonding strength. Lower adhesion of eutectic lamellae gives a weakened load transfer, lower yield strength, and stiffness [51]. Thermodynamically, the interfacial energy represents the excess free energy of an interface and is a crucial parameter of precipitation [52]. Therefore, it should be an important parameter in the formation of the $D0_{22}$ precipitate during aging. When the volume fraction of the $D0_{22}$ phase exceeds 50 % with aging for at least 6 h, primary FCC-Laves interfaces are largely replaced by FCC-$D0_{22}$ boundary (Fig. 7). This interfacial reconfiguration substantially reduces the lattice misfit from 17.7 % to 1.4 %, meanwhile enhancing the interfacial bonding and improving interface stability, as theoretically confirmed by the reduction in interfacial energy from 1.64 J/m^2 to 0.12 J/m^2. Therefore, the increased capacity for accommodating localized strain contributes to doubled plasticity of FCC-Laves EHEAs.

4.3. Deformation mechanisms induced by phase transformation

TEM analysis was performed on fractured specimens to characterize the deformation microstructure, as shown in Fig. 13. In eutectic alloys, plastic deformation typically initiates within the soft lamellae, subsequently leading to increasing strain mismatches and heterogeneous deformation fields at phase boundaries. Overlarge lattice misfit can easily induce stress accumulation and strain incompatibility at these lamellae interfaces [14,53], thereby causing poor plasticity. In AG-0.1h alloy, the plastic deformation is primarily dominated by planar dislocation slip and tiny SFs within the FCC lamellae (Fig. 13a), whereas no defects can be detected within the hard Laves lamellae, indicating a significant disparity in deformability between the two phases. The soft FCC lamellae are constrained by adjacent hard Laves phases, restricting plastic flow and leading to large local strain accumulation. To maintain strain continuity, plastic strain gradients develop near the lamella interfaces [54], which are accommodated through the storage of geometrically necessary dislocations (GNDs). This process inevitably generates long-range back-stress [55] that impedes dislocation motion in FCC lamellae until Laves lamellae start to deform concurrently (Fig. 13b), thus critically preceding crack initiation. Additionally, some $L1_2$ precipitates enriched in Ni and Ta are observed in planar arrays (Fig. 13c), similar to those reported in Ni-rich alloys [56]. These $L1_2$ precipitates are often associated with SFs [56] and could induce further stress concentrations. The deformation mechanisms in AG-1.5h alloy (Fig. 13d and e) closely resemble those in AG-0.1h alloy, with dislocations and SFs dominating until interfacial stress accumulation induces fracture. Nonetheless, the plasticity of AG-1.5h alloy is slightly improved, attributing to the presence of more deformable $D0_{22}$ precipitates that help alleviate interfacial stresses by absorption or transfer to the neighboring FCC lamellae. Furthermore, the $L1_2$ precipitate density reaches a maximum in AG-1.5h alloy among all aged conditions

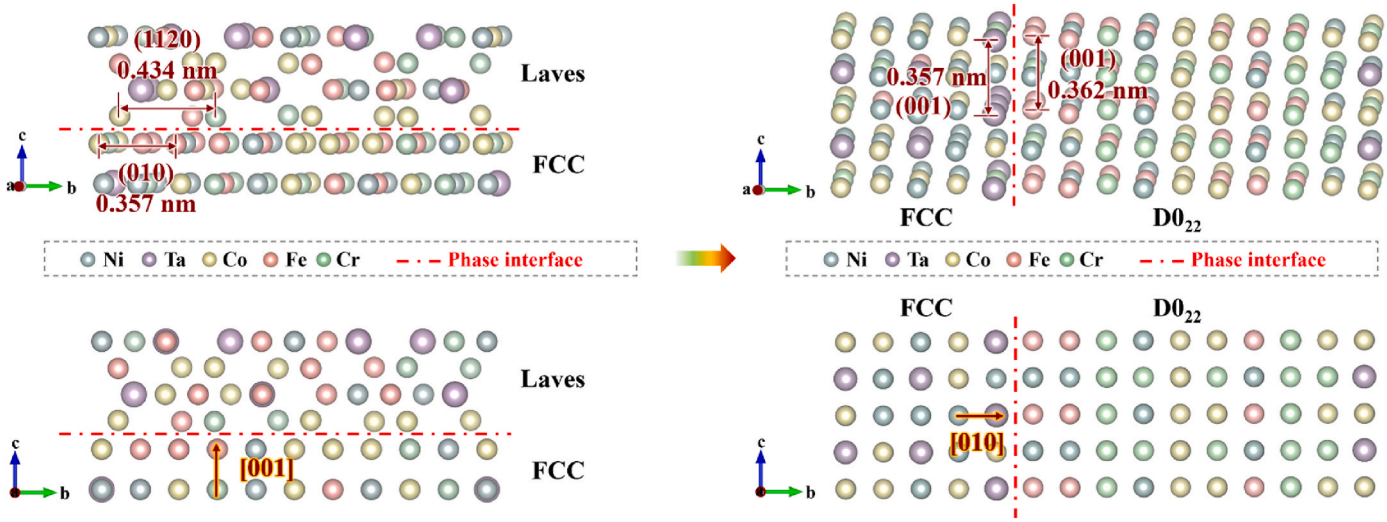

Fig. 12. FCC-Laves and FCC-$D0_{22}$ interfaces unit cell model.

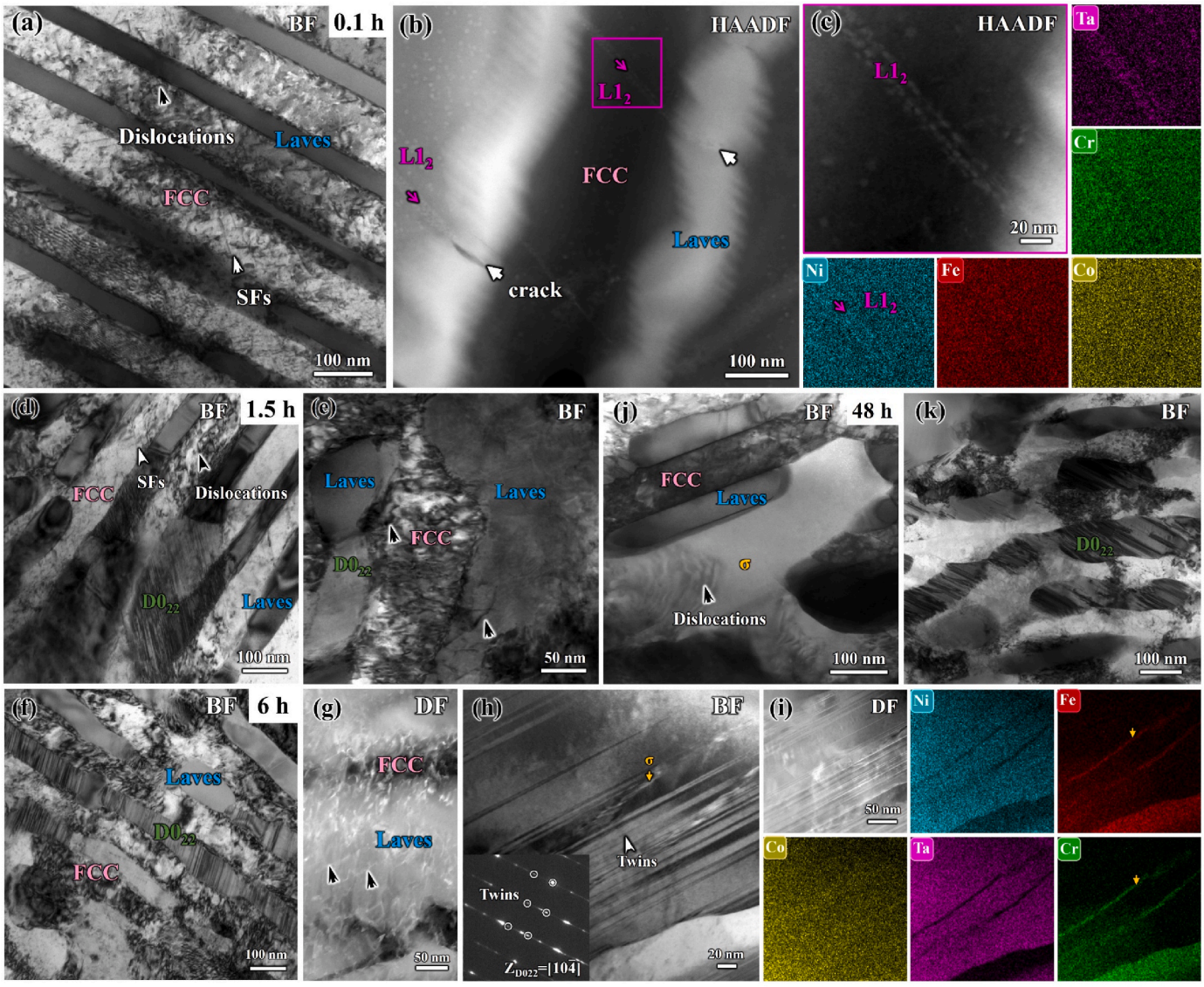

Fig. 13. Deformation structures in AG-0.1h, AG-1.5h, AG-6h and AG-48h alloys. Dislocation and SFs are observed in AG-0.1h, AG-1.5h, and AG-48h alloys, while the twins are confirmed additionally in AG-6h alloy.

(Fig. 4), which contributes to an enhanced strength.

The volume fraction of $D0_{22}$ precipitates approaches ~50 % in AG-6 alloy (Figs. 7 and 13f), prompting substantial elemental redistribution within the Laves lamellae. Specifically, Ni and Ta contents decrease due to their incorporation into $D0_{22}$ precipitates, whereas Co and Fe concentrations increase (Table 1). This compositional evolution may reduce the critical resolved shear stress for basal slip and facilitate dislocation glide in the Laves lamellae [57], as directly confirmed by TEM results in Fig. 13g. Notably, the FCC-Laves interface is progressively replaced by FCC-$D0_{22}$ boundaries driven by the phase-selective transformations. These newly formed interfaces have low misfits and high stability, enabling them to accommodate more lattice distortion. Simultaneously, additional twinning systems are activated in the $D0_{22}$ precipitates (Fig. 13h), which is expected to contribute to the increased work hardening, consistent with behaviors reported in other material systems [58,59]. The formation of deformation twins introduces new boundaries that lead to a dynamic Hall-Petch effect, which effectively reduces the mean free path of dislocations [60,61] and promotes interactions with σ precipitates (Fig. 13i), thereby contributing to strength enhancement. In AG-48h alloy, active dislocations observed in σ phases (Fig. 13j) confirm its better deformability than the Laves phase, and their concurrent deformation with strain-accommodating $D0_{22}$ precipitates (Fig. 13k) enhances plastic deformability but reduces yield strength. Fig. 14a–c shows the evolution of SFs in FCC lamellae, while Fig. 14d–f presents SFs and twins in the $D0_{22}$ phase during aging. Specifically, the FCC lamellae in AG-48h alloy exhibit the highest SF density with SFs activated along multiple crystallographic directions. In contrast, the $D0_{22}$ phase in AG-6h alloy shows the highest twin density, as also observed in the deformation microstructure (Fig. 13h).

To analyze the deformation mechanisms, the theoretical concept of the generalized stacking fault energy (GSFE) is typically employed to quantify the energy penalty for shearing specific slip systems [62]. The stable and unstable stacking fault energies (SFEs) derived from GSFE curves provide an evaluation approach in determining nanoscale plastic deformation modes within the thermally nonactivated limit. The GSFE is a function of displacement [63] for sequential fault pathways on close-packed planes

$$\gamma = \left(E\text{-}E_{perfect}\right) / A \tag{4}$$

where E and $E_{perfect}$ are the energies of configurations with and without the fault, and A is the area of the fault plane. The GSFEs were stimulated

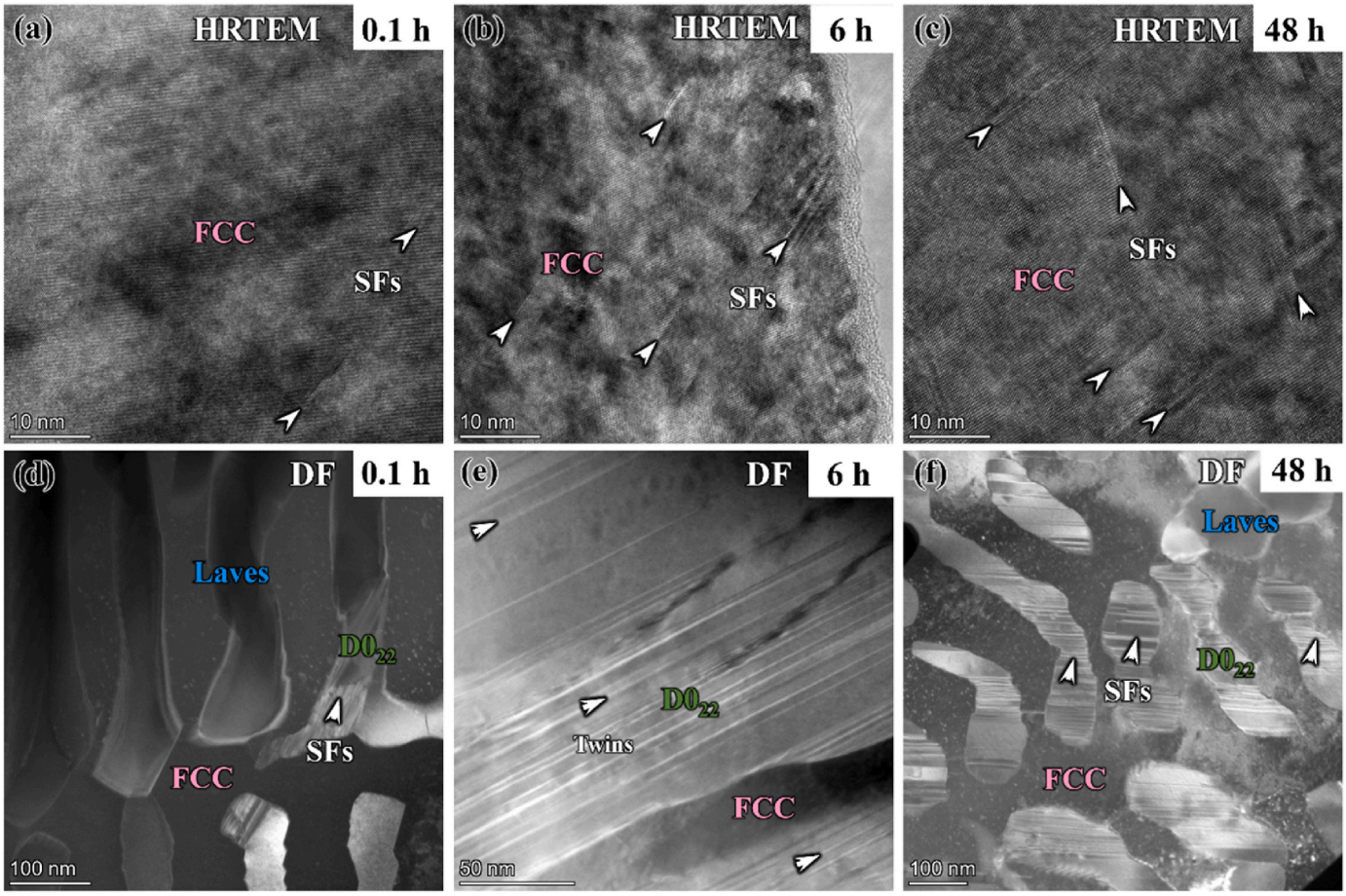

Fig. 14. SFs and Twins in AG-0.1h, AG-6h, and AG-48h alloys. (a–c) SFs in the FCC lamellae. (d–f) SFs and twins in the $D0_{22}$ phase.

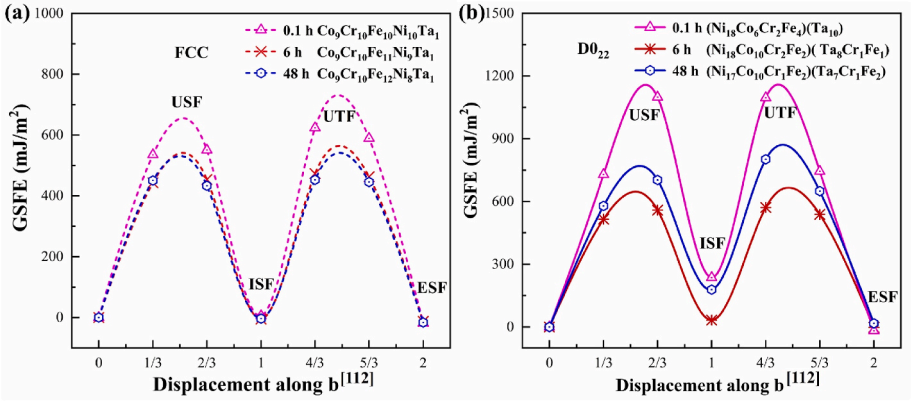

Fig. 15. GSFE (generalized stacking fault energy) curves of AG-0.1h, AG-6h, and AG-48h alloys. The GSFE curve along (a) $[112]_{FCC}$ and (b) $[112]_{D022}$ directions. The USF, ISF, UTF, and ESF represent the unstable stacking fault, intrinsic stacking fault, unstable twining energy, and extrinsic stacking fault, respectively.

in three aged alloys (AG-0.1h, AG-1.5h, and AG-48h) for the FCC and $D0_{22}$ phases with varying compositions. We focus on the GSFEs associated with dislocation slip on $\{111\}_{FCC}$, $\{001\}_{D022}$ planes and $[112]_{FCC}$, $[112]_{D022}$ directions, shown in Fig. 15. The first energy maximum determines the unstable stacking fault energy (γ_{USF}), representing the energy barrier for nucleating a partial dislocation, where it occurs at a shear displacement of around $1/2\ \vec{b}$. With continuous shearing, partial dislocation starts to propagate and leave a stable SFE (γ_{ISF}), as characterized by the first energy minimum. Along the twinning fault pathway (from 1 $\vec{b}$ to 2 $\vec{b}$), the initial configuration is an intrinsic or stable structure. The second maximum energy on the GSFE curve is the unstable-twinning SFE (γ_{UTF}), which denotes the lowest energy barrier for forming an extrinsic stacking fault or a 2-layer twin nucleus. The second minimum energy represents the two-layer twinning or extrinsic stable stacking fault (γ_{ESF}).

In the FCC lamellae, three alloys exhibit close γ_{ISF} and γ_{ESF}, with slight variation in γ_{USF} and γ_{UTF}. Although elevated γ_{ISF} and γ_{UTF} values in AG-0.1 h alloy tend to suppress SF formation, the deformation mechanisms in the matrix remain consistent in AG-6h and AG-48h alloys (Figs. 13 and 14). In contrast, the $D0_{22}$ phase shows the highest fault energies in AG-0.1h alloy, while the AG-48h and AG-6h alloys exhibit

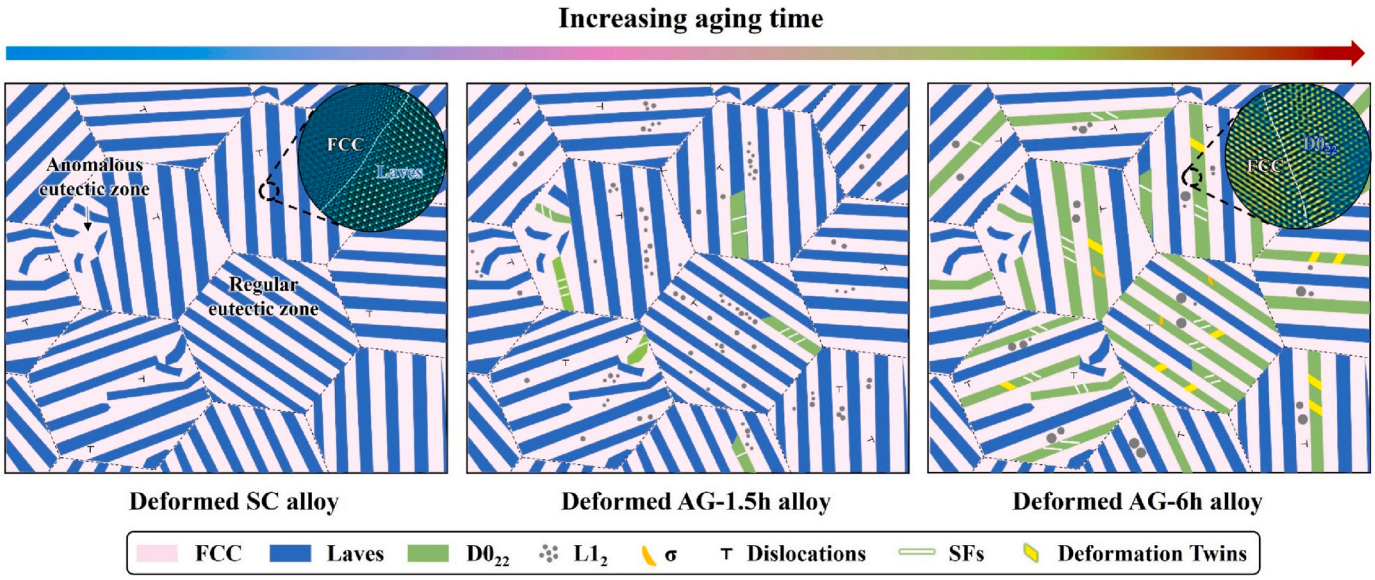

Fig. 16. Schematic diagrams of microstructural evolution and deformation mechanisms.

the medium, minimum values, respectively. Correspondingly, the deformation behavior of the $D0_{22}$ phases in AG-6h alloy is different from that in AG-0.1h and AG-48h alloys, with twinning becoming a dominant deformation mode. This change is attributed to the lowest γ_{UTF} value, which is completely consistent with the experimental results in Figs. 13 and 14. Thus, thermal-activated diffusion during phase transformations modifies GSFE, thereby governing the competition between dislocation slip and twinning in plastic deformation. Based on these discussions, the schematic diagrams of the microstructural evolutions and deformation mechanisms across varying aging times are summarized in Fig. 16. Since compression tests cannot directly assess tensile ductility, we performed tensile tests on specimens with dimensions of 10 mm (gauge length) × 2.5 mm (width) × 1 mm (thickness). However, all specimens fractured prior to yielding, demonstrating that tensile testing is not viable for this material. In the future, a number of strategies must be explored to enhance the tensile plasticity of this material. Nonetheless, the observed phase-selective transformation and interface evolution mechanisms provide valuable insights for the development of next-generation advanced structural materials.

5. Conclusion

In this study, we present the development of local coherent interfaces in FCC-Laves $CoCrFeNiTa_{0.4}$ EHEAs by selective phase transformation, exhibiting a good balance of strength and plasticity. The precipitation behaviors, interfacial relationships, mechanical properties, and deformation mechanisms were thoroughly investigated. The main findings are as follows:

1) Compared with the SC sample, the plastic strain of AG-6h alloy was increased from 5.6 % to 12 %, and the compressive strength was enhanced from 2580 MPa to 2986 MPa. Notably, the AG-6h alloy possesses a good strength-plasticity synergy among the reported aged EHEAs.
2) Aging at 1023 K for 6 h, a mass of cuboidal $L1_2$ and lamellar $D0_{22}$ transformations, chemically driven by the uphill diffusion, were observed in the FCC and Laves lamellae, respectively. Both phase transformations establish coherent interfaces with the FCC matrix. The nanoscale $L1_2$ precipitates have coherent interfaces entirely within FCC lamellae, whereas the larger $D0_{22}$ precipitates, replacing partial Laves lamellae, generate direct coherent boundaries with adjacent FCC lamellae.
3) When the aging time increases from 0.1 h to 6 h, the deformation mechanisms change from the FCC dislocation-dominant mechanisms to FCC/$D0_{22}$ SF/twins-controlled modes, indicating the reduced SFE. A deformation fundamental for coherent heterostructures is elucidated: beyond directly contributing to strength, hetero-zone interaction and the development of long-range internal stress could assist in invoking plastic mechanisms.
4) First-principles calculations on the formation energies, interfacial energies, and GSFE curves reveal that selective phase transformation is reliable for designing the low lattice misfit interfaces and high-performance materials for structural applications.

CRediT authorship contribution statement

Yusha Luo: Writing – original draft, Visualization, Methodology, Formal analysis, Data curation, Conceptualization. **Qihan Zheng:** Investigation, Formal analysis. **Bo Sun:** Writing – review & editing, Software, Conceptualization. **Ruixin Sheng:** Software, Methodology, Data curation. **Jinxiong Hou:** Methodology, Formal analysis. **Zhenzeng Chong:** Validation, Conceptualization. **Qianqian Wang:** Writing – review & editing, Supervision, Methodology, Funding acquisition. **Zhijun Guo:** Validation, Conceptualization. **Zhe Jia:** Resources, Methodology, Conceptualization. **Yang Tong:** Writing – review & editing, Supervision, Resources, Methodology. **Baolong Shen:** Writing – review & editing, Supervision, Resources, Project administration, Funding acquisition.

Declaration of competing interest

The authors declare that they have no known competing financial interests or personal relationships that could have appeared to influence the work reported in this paper.

Acknowledgments

This work was supported by the National Natural Science Foundation of China (52231005, 52571183, 52371164), the Start-up Research Fund of Southeast University (RF1028623100), Taishan Scholars Program of Shandong Province (tsqn202103052). Thank you for the technical support provided by Phadcalc (www.phadcalc.com).

Data availability

Data will be made available on request.

References

[1] H.T. Angus, Cast Iron: Physical and Engineering Properties, Butterworths, 1976.
[2] V.S. Zolotorevsky, N.A. Belov, M.V. Glazoff, Casting Aluminum Alloys, Elsevier, Amsterdam, 2007.
[3] C.S. Tiwary, P. Pandey, S. Sarkar, R. Das, S. Samal, K. Biswas, K. Chattopadhyay, Five decades of research on the development of eutectic as engineering materials, Prog. Mater. Sci. 123 (2022) 100793.
[4] Y. Lu, X. Gao, L. Jiang, Z. Chen, T. Wang, J. Jie, H. Kang, Y. Zhang, S. Guo, H. Ruan, Y. Zhao, Z. Cao, T. Li, Directly cast bulk eutectic and near-eutectic high entropy alloys with balanced strength and ductility in a wide temperature range, Acta Mater. 124 (2017) 143–150.
[5] Y.P. Lu, Y. Dong, S. Guo, L. Jiang, H. Kang, T. Wang, B. Wen, Z. Wang, J. Jie, Z. Cao, H. Ruan, T. Li, A promising new class of high-temperature alloys: eutectic high-entropy alloys, Sci. Rep. 4 (2014) 6200.
[6] Y. Lu, Y. Dong, H. Jiang, Z. Wang, Z. Cao, S. Guo, T. Wang, T. Li, P.K. Liaw, Promising properties and future trend of eutectic high entropy alloys, Scr. Mater. 187 (2020) 202–209.
[7] J. Ren, Y. Zhang, D. Zhao, Y. Chen, S. Guan, Y. Liu, L. Liu, S. Peng, F. Kong, J. D. Poplawsky, G. Gao, T. Voisin, K. An, Y.M. Wang, K.Y. Xie, T. Zhu, W. Chen, Strong yet ductile nanolamellar high-entropy alloys by additive manufacturing, Nature 608 (2022) 62–68.
[8] Q. Wei, X. Xu, Q. Shen, G. Luo, J. Zhang, J. Li, Q. Fang, C.-T. Liu, M. Chen, T.-G. Nieh, J. Chen, Metal-carbide eutectics with multiprincipal elements make superrefractory alloys, Sci. Adv. 8 (2022) 2068.
[9] P.J. Shi, R.G. Li, Y. Li, Y.B. Wen, Y.B. Zhong, W.L. Ren, Z. Shen, T.X. Zheng, J. C. Peng, X. Liang, P.F. Hu, N. Min, Y. Zhang, Y. Ren, P.K. Liaw, D. Raabe, Y. D. Wang, Hierarchical crack buffering triples ductility in eutectic herringbone high-entropy alloys, Science 373 (2021) 912–918.
[10] Q.F. Wu, F. He, J.J. Li, H.S. Kim, Z.J. Wang, J.C. Wang, Phase-selective recrystallization makes eutectic high-entropy alloys ultra-ductile, Nat. Commun. 13 (2022) 4697.
[11] Q. Cheng, Y. Zhang, X.D. Xu, D. Wu, S. Guo, T.G. Nieh, J.H. Chen, Mechanistic origin of abnormal annealing-induced hardening in an $AlCoCrFeNi_{2.1}$ eutectic multi-principal-element alloy, Acta Mater. 252 (2023) 118905.
[12] H. Ge, W. Xing, B. Chen, X. Hu, S. Zheng, K. Liu, X. Ma, A new refractory Ni_7Nb_2 phase identified in Laves eutectic regions by TEM study, Acta Mater. 214 (2021) 116985.
[13] Y. Jia, Z. Wang, Q. Wu, Y. Wei, X. Bai, L. Liu, J. Wang, X. Liu, L. Wang, F. He, J. Li, J. Wang, Boron microalloying for high-temperature eutectic high-entropy alloys, Acta Mater. 262 (2024) 119427.
[14] P. Shi, W. Ren, T. Zheng, Z. Ren, X. Hou, J. Peng, P. Hu, Y. Gao, Y. Zhong, P. K. Liaw, Enhanced strength-ductility synergy in ultrafine-grained eutectic high-entropy alloys by inheriting microstructural lamellae, Nat. Commun. 10 (2019) 489.
[15] X. Gao, Y. Lu, B. Zhang, N. Liang, G. Wu, G. Sha, J. Liu, Y. Zhao, Microstructural origins of high strength and high ductility in an $AlCoCrFeNi_{2.1}$ eutectic high-entropy alloy, Acta Mater. 141 (2017) 59–66.
[16] H. Jiang, D. Qiao, W. Jiao, K. Han, L. Yiping, P.K. Liaw, Tensile deformation behavior and mechanical properties of a bulk cast $Al_{0.9}CoFeNi_2$ eutectic high-entropy alloy, J. Mater. Sci. Technol. 61 (2021) 119–124.
[17] T. Xiong, W. Yang, S. Zheng, Z. Liu, Y. Lu, R. Zhang, Y. Zhou, X. Shao, B. Zhang, J. Wang, F. Yin, P.K. Liaw, X. Ma, Faceted Kurdjumov-Sachs interface-induced slip continuity in the eutectic high-entropy alloy, $AlCoCrFeNi_{2.1}$, J. Mater. Sci. Technol. 65 (2021) 216–227.
[18] F. Chu, D.J. Thoma, Phase stability and defect structure of the C15 Laves phase, Acta Mater. 46 (1998) 1759–1769.
[19] Z.Q. Yang, M.F. Chisholm, B. Yang, X.L. Ma, Y.J. Wang, M.J. Zhuo, S.J. Pennycook, Role of crystal defects on brittleness of C15 Cr_2Nb Laves phase, Acta Mater. 60 (2012) 2637–2646.
[20] P.K. Ojha, S. Yoshida, U. Sunkari, B. Tripathy, N. Tsuji, P.P. Bhattacharjee, Highly deformable Laves phase in a high entropy alloy, Scr. Mater. 240 (2024) 115828.
[21] M. Tanimura, Y. Koyama, The role of antiphase boundaries in the kinetic process of the $L1_2 \rightarrow D0_{22}$ structural change of an $Ni_3Al_{0.45}V_{0.50}$ alloy, Acta Mater. 54 (2006) 4385–4391.
[22] F. He, D. Chen, B. Han, Q.F. Wu, Z.J. Wang, S.L. Wei, D.X. Wei, J.C. Wang, C.T. Liu, J.-J. Kai, Design of $D0_{22}$ superlattice with superior strengthening effect in high entropy alloys, Acta Mater. 167 (2019) 275–286.
[23] L. Fan, T. Yang, Y. Zhao, J. Luan, G. Zhou, H. Wang, Z. Jiao, C.T. Liu, Ultrahigh strength and ductility in newly developed materials with coherent nanolamellar architectures, Nat. Commun. 11 (2020) 6240.
[24] J.M. Oblak, D.F. Paulonis, D.S. Duvall, Coherency strengthening in Ni base alloys hardened by $D0_{22}$ precipitates, Metall. Trans. A 5 (1974) 143–153.
[25] A. Suzuki, H. Kojima, T. Matsuo, M. Takeyama, Alloying effect on stability of multi-variant structure of Ni_3V at elevated temperatures, Intermetallics 12 (2004) 969–975.
[26] Y. Huang, Z. Mao, R.D. Noebe, D.N. Seidman, The effects of refractory elements on Ni-excesses and Ni-depletions at γ(f.c.c.)/$\gamma'(L1_2)$ interfaces in model Ni-based superalloys: Atom-probe tomographic experiments and first-principles calculations, Acta Mater. 121 (2016) 288–298.
[27] Y. Lu, H. Jiang, S. Guo, T. Wang, Z. Cao, T. Li, A new strategy to design eutectic high-entropy alloys using mixing enthalpy, Intermetallics 91 (2017) 124–128.
[28] N. Saunders, Z. Guo, X. Li, A.P. Miodownik, J.-P. Schillé, Using JMatPro to model materials properties and behavior, JOM 55 (2003) 60–65.
[29] N. Saunders, M. Fahrmann, C.J. Small, The application of CALPHAD calculation to Ni-based superalloys, Superalloys (2000) 803–811.
[30] G. Kresse, J. Furthmuller, Efficient iterative schemes for ab initio total-energy calculations using a plane-wave basis set, Phys. Rev. B 54 (1996) 11169–11186.
[31] J.P. Perdew, K. Burke, M. Ernzerhof, Generalized gradient approximation made simple, Phys. Rev. Lett. 77 (1996) 3865–3868.
[32] T. Yang, Y.L. Zhao, Y. Tong, Z.B. Jiao, J. Wei, J.X. Cai, X.D. Han, D. Chen, A. Hu, J. J. Kai, K. Lu, Y. Liu, C.T. Liu, Multicomponent intermetallic nanoparticles and superb mechanical behaviors of complex alloys, Science 362 (2018) 933–937.
[33] G. Kresse, D. Joubert, From ultrasoft pseudopotentials to the projector augmented-wave method, Phys. Rev. B 59 (1999) 1758–1775.
[34] W. Shao, Y. Zhou, L. Rao, X. Xing, Z. Shi, Q. Yang, Effect of Cr doping on interface properties of DLC/CrN composite coatings: first-principles study, Diam. Relat. Mater. 121 (2022) 108721.
[35] Z. Li, Q. Lv, H. Wei, M. Zhou, F. Zhang, Q. Shan, Effects of RE (Nd, Ce, Y, La) on TiC (100)/Fe(110) interface based on first-principles calculations, Vacuum 205 (2022) 111449.
[36] M. Methfessel, A.T. Paxton, High-precision sampling for Brillouin-zone integration in metals, Phys. Rev. B 40 (1989) 3616–3621.
[37] R. Krishna, Uphill diffusion in multicomponent mixtures, Chem. Soc. Rev. 44 (2015) 2812–2836.
[38] B.L. Bramfitt, The effect of carbide and nitride additions on the heterogeneous nucleation behavior of liquid iron, Mater. Trans. 1 (1970) 1970–1987.
[39] L. Liu, Y. Zhang, J. Li, M. Fan, X. Wang, G. Wu, Z. Yang, J. Luan, Z. Jiao, C.T. Liu, P. K. Liaw, Z. Zhang, Enhanced strength-ductility synergy via novel bifunctional nano-precipitates in a high-entropy alloy, Int. J. Plast. 153 (2022) 103235.
[40] M.C. Niu, S. Qiu, Q. Yu, W. Li, S.Z. Zhang, J.M. Guo, J.H. Luan, W. Wang, T. Yang, X.L. Wang, Z.B. Jiao, Achieving excellent elevated-temperature mechanical properties in dual-phase high-entropy alloys via nanoscale co-precipitation and heterostructure engineering, Acta Mater. 284 (2025) 120634.
[41] S. Kirklin, J.E. Saal, B. Meredig, A. Thompson, J.W. Doak, M. Aykol, S. Rühl, C. Wolverton, The open quantum materials database (OQMD): assessing the accuracy of DFT formation energies, npj Comput. Mater. 1 (2015).
[42] L. Zhu, H. Bai, B. Chen, X. Sun, K. Qu, B. Xia, Microplastic pollution in North Yellow Sea, China: observations on occurrence, distribution and identification, Sci. Total Environ. 636 (2018) 20–29.
[43] D.C. Lv, D. McAllister, M.J. Mills, Y. Wang, Deformation mechanisms of $D0_{22}$ ordered intermetallic phase in superalloys, Acta Mater. 118 (2016) 350–361.
[44] T. M., Y. H., G.M.M. MatsuoT, Phase equilibria and microstructure controle using Ni_3Nb-δ phase in Ni-Nb-Fe ternary systems at elevated temperatures, J. Mater. Process. Technol. 117–3 (2001) D7.
[45] J.C. Zhao, M.R. Notis, Spinodal decomposition, ordering transformation, and discontinuous precipitation in a Cu-15Ni-8Sn alloy, Acta Mater. 46 (1998) 4203–4218.
[46] X. Song, Y. Han, X. Wang, W. Liu, J. Wu, H. Cui, First-principles study of adhesion strength and stability of the TiB_2/TiC interface in composite materials, Ceram. Int. 44 (2018) 1756–1763.
[47] H.H. Xiong, H.N. Zhang, J.H. Dong, Adhesion strength and stability of TiB_2/TiC interface in composite coatings by first principles calculation, Comput. Mater. Sci. 127 (2017) 244–250.
[48] S. Cao, Y. Jiang, R. Yang, Q.-M. Hu, Properties of β/ω phase interfaces in Ti and their implications on mechanical properties and ω morphology, Comput. Mater. Sci. 158 (2019) 49–57.
[49] R. Benedek, D.N. Seidman, C. Woodward, The effect of misfit on heterophase interface energies, J. Phys-Condens. Mat. 14 (2002) 2877–2900.
[50] S. Lu, Q.-M. Hu, M.P.J. Punkkinen, B. Johansson, L. Vitos, First-principles study of fcc-Ag/bcc-Fe interfaces, Phys. Rev. B 87 (2013) 224104.
[51] E.A. Feest, Interfacial phenomena in metalmatrix composites, Composites 25 (1994) 75–86.
[52] M. Christensen, S. Dudiy, G. Wahnström, First-principles simulations of metal-ceramic interface adhesion: Co/WC versus Co/TiC, Phys. Rev. B 65 (2002) 045408.
[53] M. Wang, Y. Lu, J. Lan, T. Wang, C. Zhang, Z. Cao, T. Li, P.K. Liaw, Lightweight, ultrastrong and high thermal-stable eutectic high-entropy alloys for elevated-temperature applications, Acta Mater. 248 (2023) 118806.
[54] K. Lu, Making strong nanomaterials ductile with gradients, Science 345 (2014) 1455–1456.
[55] E. Ma, T. Zhu, Towards strength–ductility synergy through the design of heterogeneous nanostructures in metals, Mater. Today 20 (2017) 323–331.
[56] I. Kirman, D.H. Warrington, The Precipitation of Ni_3Nb phases in a Ni-Fe-Cr-Nb alloy, Metall. Trans. A 1 (1970) 2667–2675.
[57] Y. Xue, N. Takata, H. Li, M. Kobashi, L. Yuan, Critical resolved shear stress of activated slips measured by micropillar compression tests for single-crystals of Cr-based Laves phases, Mater. Sci. Eng., A 806 (2021) 140861.
[58] H. Beladi, I.B. Timokhina, Y. Estrin, J. Kim, B.C. De Cooman, S.K. Kim, Orientation dependence of twinning and strain hardening behaviour of a high manganese twinning induced plasticity steel with polycrystalline structure, Acta Mater. 59 (2011) 7787–7799.
[59] L. Remy, A. Pineau, Twinning and strain-induced FCC to HCP transformation in the Fe-Mn-Cr-C system, Mater. Sci. Eng. 28 (1977) 99–107.
[60] I. Gutierrez-Urrutia, D. Raabe, Dislocation and twin substructure evolution during strain hardening of an Fe-22wt.% Mn-0.6wt.% C TWIP steel observed by electron channeling contrast imaging, Acta Mater. 59 (2011) 6449–6462.

[61] F. Otto, Y. Yang, H. Bei, E.P. George, Relative effects of enthalpy and entropy on the phase stability of equiatomic high-entropy alloys, Acta Mater. 61 (2013) 2628–2638.
[62] V. Vítek, Intrinsic stacking faults in body-centred cubic crystals, Philos. Mag. 18 (1968) 773–786.
[63] S. Ogata, J. Li, S. Yip, Ideal pure shear strength of Aluminum and Copper, Science 298 (2002) 807.
[64] A.V. Kazantzis, M. Aindow, I.P. Jones, G.K. Triantafyllidis, J.T.M. De Hosson, The mechanical properties and the deformation microstructures of the C15 Laves phase Cr_2Nb at high temperatures, Acta Mater. 55 (2007) 1873–1884.
[65] F. He, Z. Wang, X. Shang, C. Leng, J. Li, J. Wang, Stability of lamellar structures in $CoCrFeNiNb_x$ eutectic high entropy alloys at elevated temperatures, Mater. Des. 104 (2016) 259–264.
[66] X. Ye, Z. Cheng, C. Liu, X. Wu, L. Yu, M. Liu, D. Fang, G. Zhao, B. Li, The microstructure and properties of $Fe_{55}Cr_{15}Ni_{(30-x)}Nb_x$ eutectic high-entropy alloys, Mater. Sci. Eng., A 841 (2022) 143026.
[67] L. Jiang, Y. Lu, Y. Dong, T. Wang, Z. Cao, T. Li, Effects of Nb addition on structural evolution and properties of the $CoFeNi_2V_{0.5}$ high-entropy alloy, Appl. Phys. A 119 (2015) 291–297.
[68] L. Jiang, Y. Lu, W. Wu, Z. Cao, T. Li, Microstructure and mechanical properties of a $CoFeNi_2V_{0.5}Nb_{0.75}$ eutectic high entropy alloy in as-cast and heat-treated conditions, J. Mater. Sci. Technol. 32 (2016) 245–250.
[69] M. Zhu, L. Yao, Y. Liu, M. Zhang, K. Li, Z. Jian, Microstructure evolution and mechanical properties of a novel $CrNbTiZrAl_x$ ($0.25 \leq x \leq 1.25$) eutectic refractory high-entropy alloy, Mater. Lett. 272 (2020) 127869.
[70] X. Lin, M. Wang, G. Ren, D. Qiao, Y. Lu, T. Wang, T. Li, Microstructure evolution and mechanical properties of $CrFeNiXV_{0.64}Ta_{0.36}$ eutectic high-entropy alloys, Mater. Char. 181 (2021) 111449.